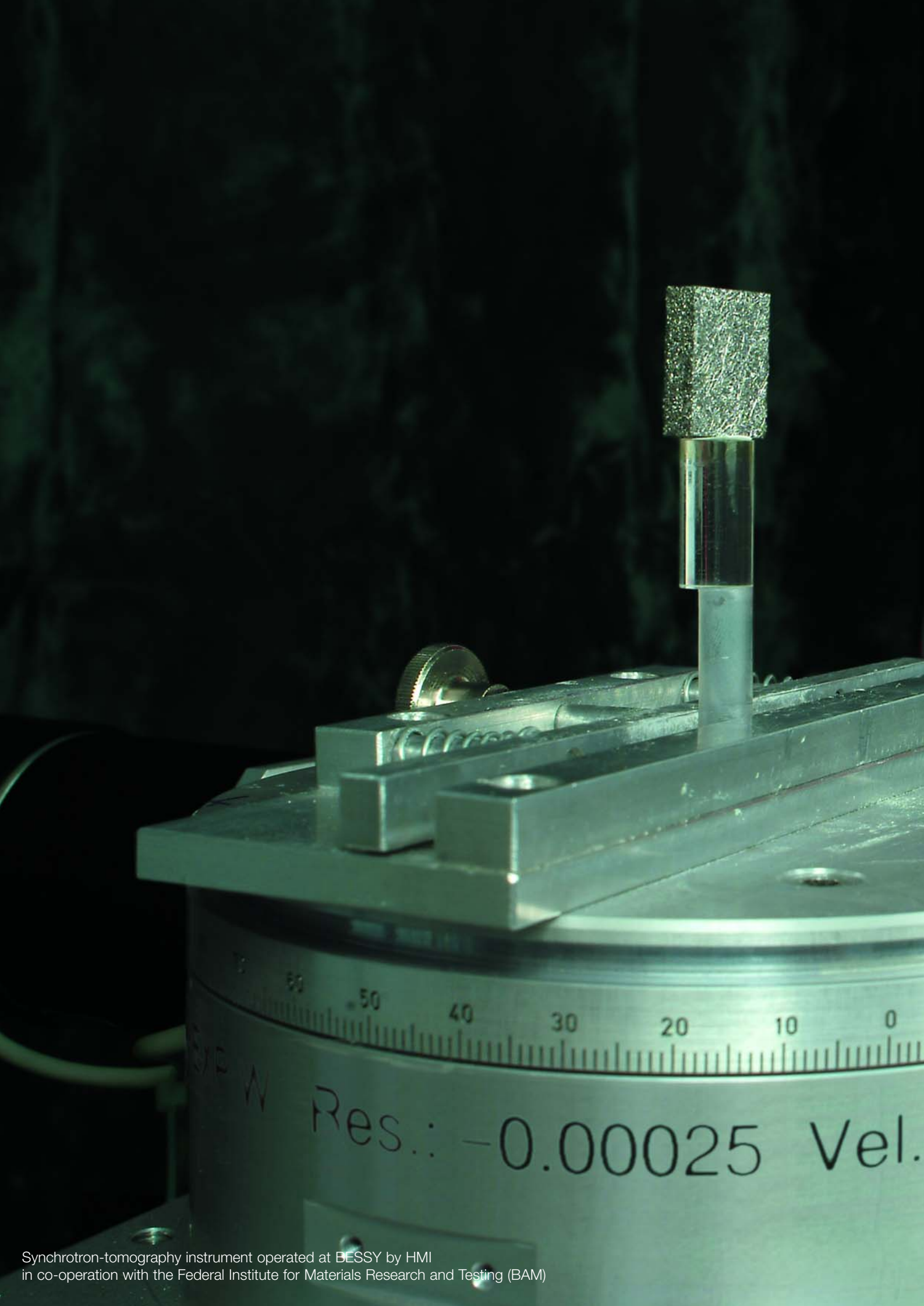


Annual Report 2003

Structural Research





Scientific highlights Structural Research 2003

BENSC User-Service	S. 28
ISL User-Service	S. 38
NAA User-Service	S. 44
SF1, Methods and Instruments	S. 46
SF2, Magnetism	S. 52
SF3, Materials	S. 56
SF4, Structure and Dynamics	S. 62
SF5, Theoretical Physics	S. 70
SF6, Molecular Trace Element Research in the Life Sciences	S. 72

Antiferromagnetic order as a competing ground state for electron-doped high-transition temperature superconductors

H. J. Kang¹, M. Matsuura², Pengcheng Dai^{1,2}, J. R. Thompson^{1,2}, J. W. Lynn³, Shou-Cheng Zhang⁴, D. N. Argyriou⁵, K. Prokeš⁵, Y. Onose⁶, Y. Tokura^{7,8}, Y. Kurita⁹, Seiki Komiya⁹, Yoichi Ando⁹

■ 1 Department of Physics and Astronomy, The University of Tennessee, Knoxville, Tennessee, USA ■ 2 Condensed Matter Sciences Division, Oak Ridge National Laboratory, Oak Ridge, Tennessee, USA ■ 3 NIST, Center for Neutron Research, National Institute of Standards and Technology, Gaithersburg, Maryland, USA ■ 4 Department of Physics, Stanford University, Stanford, California, USA ■ 5 HMI, SF2 ■ 6 Spin Superstructure Project, ERATO, Japan Science and Technology, Tsukuba, Japan ■ 7 Correlated Electron Research Center, Tsukuba, Japan ■ 8 Department of Applied Physics, University of Tokyo, Tokyo, Japan ■ 9 Central Research Institute of Electric Power Industry, Komae, Tokyo, Japan

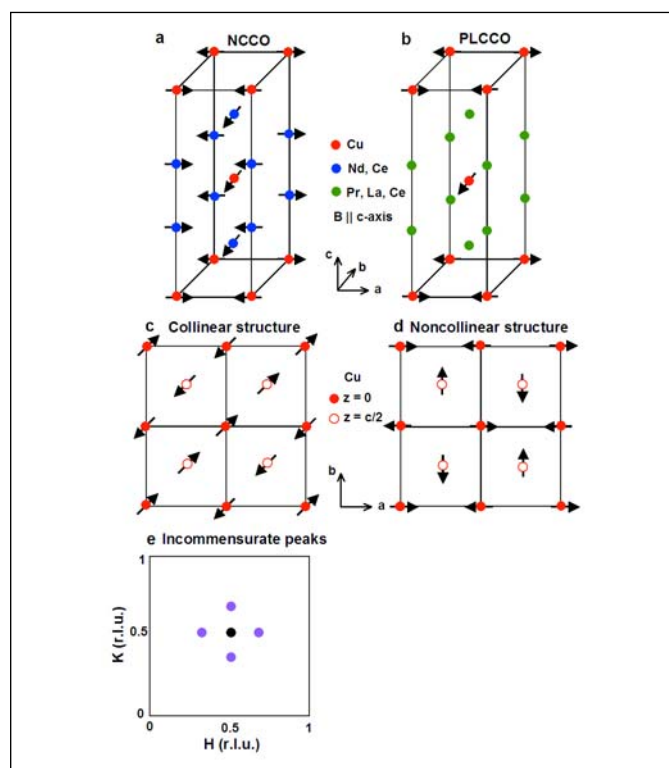


Fig. 1: Noncollinear spin structure of a) phase I/III in NCCO b) in PLCCO. The oxygen atoms are not shown for clarity. c) Collinear spin structure has the spins in adjacent layers parallel or antiparallel. d) The spins in adjacent layers are orthogonal in noncollinear structure. e) Data from neutron scattering on a copper oxide (sketch). The black circle is the Bragg peak coming from antiferromagnetism of the undoped parent compound. The pink circles are incommensurate peaks, which are shifted away from AF Bragg peaks. The incommensurate peaks reflect a periodic structure with a period slightly differing from the period of the crystal. Here, these peaks are associated with the separation of holes, when holes are doped.

The discovery of high-transition temperature (high- T_c) superconductivity in copper oxides (cuprates) in 1986 created unprecedented research activities in studying these materials. The parent compounds of the high- T_c cuprates are antiferromagnetic Mott insulators [1]. The crystal structure of these materials is distinguished by typical CuO_2 planes. Each Cu^{2+} in such a plane has one unpaired electron and the spins of these electrons form an antiferromagnetic long-range order. When holes or electrons are doped into these planes, the long-range antiferromagnetic ordered phase is destroyed and the copper oxide materials become metallic and superconducting with persistent short-range antiferromagnetic spin correlations. Much work has focused on understanding the interplay between magnetism and superconductivity [1], because spin fluctuations may mediate electron pairing for superconductivity. Soon after the discovery of hole-doped superconductors, Tokura and his coworkers found the electron-doped superconductor $\text{Nd}_{2-x}\text{Ce}_x\text{CuO}_4$ (NCCO) [2]. Although both hole-doped $\text{La}_{2-x}\text{Sr}_x\text{CuO}_4$ (LSCO) and electron-doped NCCO have two-dimensional CuO_2 planes, their phase diagrams versus doping concentrations are asymmetric. For hole-doped LSCO materials, antiferromagnetism rapidly weakens with increasing doping x and is replaced by superconductivity over a wide range of x with a maximum T_c at $x = 0.15$. For electron-doped materials, as-grown materials are nonsuperconducting antiferromagnetic insulators and superconductivity can only be induced after annealing the $x > 0.11$ samples in a narrow x range. Therefore, finding the similarities and differences of the n -type and p -type cuprates would be very important in understanding the mechanism of high- T_c superconductivity.

Since high- T_c cuprates are layered materials, superconductivity is highly anisotropic and the application of a magnetic field along the direction perpendicular to the CuO_2 planes can suppress superconductivity much easier than the same field applied parallel to the CuO_2 planes. For LSCO, superconductivity coexists with incommensurate (Fig. 1e) quasi two-dimensional spin-density wave modulations in the underdoped regime, where the superconducting transition temperature T_c is below the highest value [3]. Application of a magnetic field along the c -axis enhances the static incommensurate spin-density wave order [4, 5]. Since a similar field applied in the CuO_2 plane has little effect on superconductivity and spin-density wave order [6], these results suggest that the incommensurate spin-density wave order competes with superconductivity.

For electron-doped materials, our ultimate goal is to determine if similar spin-density wave exists and, if so, to measure their magnetic field-induced effect. The Cu^{2+} spins have a simple antiferromagnetic (AF) collinear structure (Fig. 1c) in the parent compounds of hole-doped materials such as La_2CuO_4 and $\text{YBa}_2\text{Cu}_3\text{O}_6$. Below 30 K, the Cu^{2+} spins in the parent compound of electron-doped Nd_2CuO_4 and Pr_2CuO_4 form the noncollinear antiferromagnetic structure of Fig. 1a and b, due to the exchange coupling between Cu^{2+} and rare-earth ions. We use neutron scattering to investigate the magnetic field effect in electron-doped high- T_c superconductor $\text{Nd}_{1.85}\text{Ce}_{0.15}\text{CuO}_4$ [7]. However, the annealing process necessary to make superconductivity in this material also induces a cubic $(\text{Nd,Ce})_2\text{O}_3$ as an impurity phase [8]. Because Nd in $(\text{Nd,Ce})_2\text{O}_3$ has a magnetic ground state and is lattice matched with $\text{Nd}_{1.85}\text{Ce}_{0.15}\text{CuO}_4$ in the CuO_2 plane, application of a c -axis aligned magnetic field on $\text{Nd}_{1.85}\text{Ce}_{0.15}\text{CuO}_4$ will also induce paramagnetic scattering from $(\text{Nd,Ce})_2\text{O}_3$. For zero momentum transfer along the c -axis, the lattice from NCCO and $(\text{Nd,Ce})_2\text{O}_3$ are lattice matched. As a consequence, the results obtained in [7] may be ambiguous [8] and are subject to debate [9].

There are two ways to resolve this impurity problem and determine the intrinsic properties of electron-doped materials. First, even though the lattice parameters of the cubic impurity $(\text{Nd,Ce})_2\text{O}_3$ are lattice matched with NCCO in the ab -plane, its c -axis lattice constant is about 10% smaller than that of NCCO. This lattice constant mismatch gives incommensurate scattering in NCCO at positions such as $(0.5,$

$0.5, L)$ $L=2.2, 4.4$, and so on. Therefore, one can separate the impurity scattering by simply performing a c -axis aligned magnetic field experiment at non-zero integer L positions, such as $L = 1, 2$, and 3 as such scattering can only arise from NCCO. To do this, we performed an experiment at HMI using the HM-2 horizontal field magnet to probe the AF order at $(0.5, 0.5, 3)$ position. The antiferromagnetic reflection $(0.5, 0.5, 3)$ of NCCO shows clearly the field-induced effect (Fig. 2a), while the impurity reflection $(2, 0, 4)$ shows no observable field-induced effect at NCCO position $(0.5, 0.5, 4.4)$ (Fig. 2b). These results unambiguously demonstrate that application of a c -axis aligned magnetic field enhances the residual antiferromagnetic order [10].

The second method to resolve this impurity issue is simply to perform field-induced experiments on samples where the impurity phase has a nonmagnetic ground state. For this purpose, we grew single crystals of $\text{Pr}_{0.88}\text{LaCe}_{0.12}\text{CuO}_4$ (PLCCO), where Pr^{3+} has a nonmagnetic singlet ground state and the impurity phase $(\text{Pr,L a,C e})_2\text{O}_3$ has no observable field-induced effect up to 12 T (see Fig. 3 b) [11]. The as-grown PLCCO has the same noncollinear Cu spin structure as phase I/III of NCCO, except a small induced Pr moment is antiparallel to the Cu moment direction. Since the rare earth Pr^{3+} moment contribution is negligible in PLCCO and the impurity phase $(\text{Pr,L a,C e})_2\text{O}_3$ does not show any field effect, PLCCO is an ideal material for investigating the phase transition from the superconducting state to the AF ordered state.

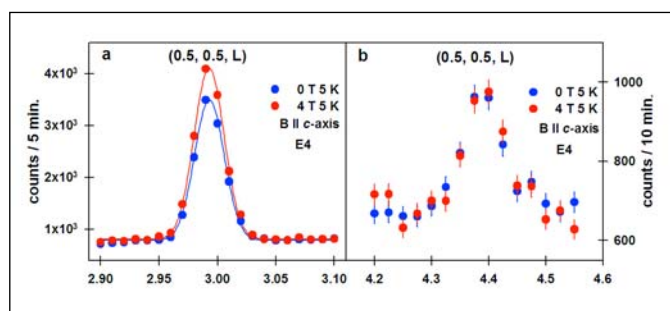


Fig. 2: The field effect on $\text{Nd}_{1.85}\text{Ce}_{0.15}\text{CuO}_4$
a) The L scan at AF position $(0.5, 0.5, 3)$ of NCCO shows that a c -axis aligned field enhances the AF order.
b) The impurity reflection $(2, 0, 4)$, which is at $(0.5, 0.5, 4.4)$ in NCCO shows no field effect.

We first investigate at zero-field how as-grown AF ordered insulator is transformed into a superconductor. We find that the existence of commensurate spin-density wave modulations in underdoped PLCCO is similar to that in LSCO [12]. We then study the effect of an applied magnetic field on spin-density wave modulations at HMI. The c -axis aligned magnetic field on $\text{Pr}_{0.88}\text{LaCe}_{0.12}\text{CuO}_4$ induces the AF order at (0.5, 0.5, 0) position (Fig. 3 a), whereas no field-induced effect is observed at (0, 0, 2.2) from impurity phase (Fig. 3 b) [11]. Therefore, it is clear that the observed field effect at (0.5, 0.5, 0) cannot arise from the impurity phase and a c -axis aligned field also affects the spin-density wave modulation in electron-doped materials.

In summary, our experiments performed using high-magnetic fields at HMI show that the spin-density wave order can be enhanced by an applied field irrespective of electron and hole doping. These results can provide quantitative constraints on theoretical understanding of the interplay between magnetism and superconductivity in high- T_c copper oxides.

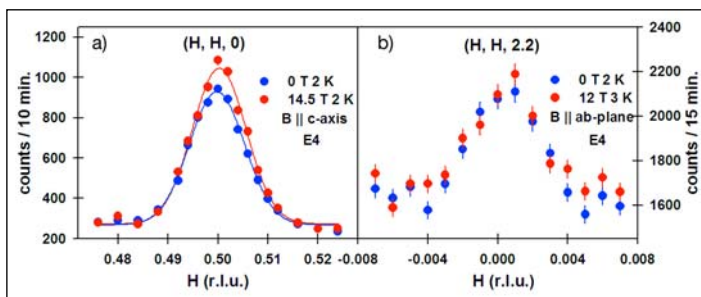


Fig. 3: The field effect on $\text{Pr}_{0.88}\text{LaCe}_{0.12}\text{CuO}_4$ a) The AF order is induced at (0.5, 0.5, 0), when superconductivity is suppressed by a field along the c -axis. b) The impurity position (0, 0, 2.2) has no field effect.

- [1] M. A. Kastner, R. J. Birgeneau, G. Shirane, and Y. Endoh, *Rev. Mod. Phys.* **70**, 897 (1998).
- [2] Y. Tokura, H. Takagi, and S. Uchida, *Nature* **337**, 345 (1989).
- [3] H. Kimura, K. Hirota, H. Matsushita, K. Yamada, Y. Endoh, S-H Lee, C. F. Majkrzak, R. Erwin, M. Greven, Y. S. Lee, M. A. Kastner, and R. J. Birgeneau, *Phys. Rev. B* **59**, 6517 (1999).
- [4] S. Katano, M. Sato, K. Yamada, T. Suzuki, and T. Fukase, *Phys. Rev. B* **62**, R14677 (2000).
- [5] B. Lake, H. M. Rønnow, N. B. Christensen, G. Aeppli, K. Lefmann, D. F. McMorrow, P. Vorderwisch, P. Smeibidl, N. Mangkorn-tong, T. Sasagawa, M. Nohara, H. Takagi, and T. E. Mason, *Nature* **415**, 299 (2002).
- [6] B. Lake, K. Lefmann, N. B. Christensen, G. Aeppli, D. F. McMorrow, P. Vorderwisch, P. Smeibidl, N. Mangkorn-tong, T. Sasagawa, M. Nohara, H. Takagi (unpublished).
- [7] H. J. Kang, Pengcheng Dai, J. W. Lynn, M. Matsuura, J. R. Thompson, Shou-Cheng Zhang, D. N. Argyriou, Y. Onose, Y. Tokura, *Nature* **423**, 522 (2003).
- [8] P. K. Mang, S. Laroche, M. Greven, *Nature* **426**, 139 (2003).
- [9] H. J. Kang, Pengcheng Dai, J. W. Lynn, M. Matsuura, J. R. Thompson, Shou-Cheng Zhang, D. N. Argyriou, Y. Onose, Y. Tokura, *Nature* **426**, 140 (2003).
- [10] M. Matsuura, Pengcheng Dai, H. J. Kang, J. W. Lynn, D. N. Argyriou, K. Prokes, Y. Onose, Y. Tokura, *Phys. Rev. B* **68**, 144503 (2003).
- [11] H. J. Kang, Pengcheng Dai, H. A. Mook, M. Matsuura, J. W. Lynn, Y. Kurita, Seiki Komiyama, Yoichi Ando, (unpublished).
- [12] H. J. Kang, Pengcheng Dai, H. A. Mook, M. Matsuura, J. W. Lynn, Y. Kurita, Seiki Komiyama, Yoichi Ando, (unpublished).
- [13] The NCCO and PLCCO samples are provided by Y. Tokura's group at The University of Tokyo and Y. Ando's group at Central Research Institute of Electric Power Industry, Komae, Tokyo 201-8511, Japan, respectively.

Neutron diffraction and theoretical model studies of the field induced magnetic phases of the $\text{ErNi}_2\text{B}_2\text{C}$ superconductor

A. Jensen^{1,2}, K. Nørgaard Toft¹, A.B. Abrahamsen¹, N.H. Andersen¹, J. Jensen², P. Hedegård², J. Klenke³, K. Prokeš³, P. Smeibidl³, S. Danilkin³ and V. Sikolenko³

■ 1 Materials Research Department, Risø National Laboratory, Roskilde, Denmark ■ 2 Ørsted Laboratory, Niels Bohr Institute fAPG, Copenhagen, Denmark ■ 3 HMI, SF 2

Introduction

Magnetism and superconductivity are two basic properties of materials that have been studied intensively for many years. While a solid understanding of magnetism has been developed during the last fifty years, there are significant basic properties that remain to be explained in superconductivity, as exemplified by the mechanism underlying high-temperature superconductivity. Superconductivity and static magnetic order are generally considered as competing phases. Back in the fifties and sixties, it was observed that superconductivity was strongly suppressed or extinguished by substitution of magnetic impurities at a 1% level [1, 2]. However, in the seventies it was revealed that true long-range magnetic order co-existed in Chevrel phase superconductors like RMO_6S_8 and the related RRh_4B_4 (R = rare earth) [3]. Here it is argued that the detrimental effect of the rare earth ions is avoided, because they form a fully ordered sublattice that is isolated from the conduction electrons. Furthermore, the ordering sets in at rather low temperature (approximately 1 K) and has a modulated structure that averages out on a length scale of the superconducting order parameter. In the late eighties all attention was given to the high-temperature superconductors where highly interesting, but so far unraveled, interactions exist between the magnetic and the superconducting electrons or holes within the same copper-oxide planes.

The rare-earth nickel boron-carbides $\text{RNi}_2\text{B}_2\text{C}$ have attracted much attention after their discovery in 1994 [4, 5], because superconductivity and antiferromagnetism co-exist for $\text{R} = \text{Dy}, \text{Ho}, \text{Er}$ and Tm at comparable temperatures $6 \text{ K} \leq T_c \leq 11 \text{ K}$ and $1.7 \text{ K} \leq T_N \leq 11 \text{ K}$ [6]. Here, T_N is the Néel temperature. Above this temperature, the antiferromagnetic order in a crystal is lost, similarly to the superconducting properties that are lost above the critical temperature T_c . $\text{ErNi}_2\text{B}_2\text{C}$, in particular, is interesting be-

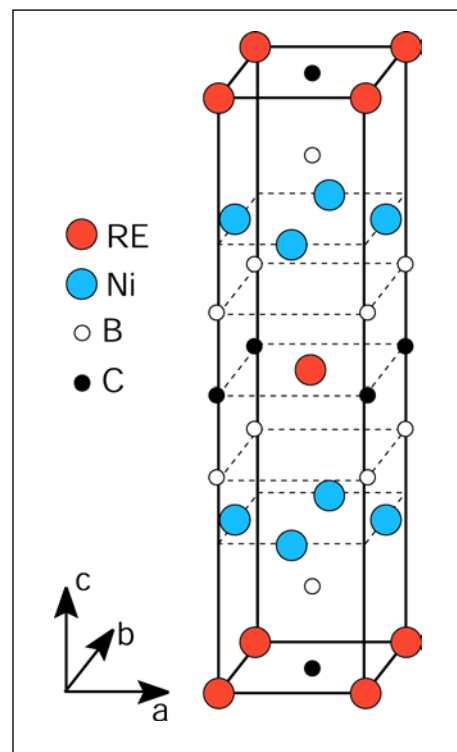


Fig. 1: Crystal structure of the rare-earth borocarbides

cause magnetization studies have indicated weak ferromagnetism below $T_c = 2.3 \text{ K}$ in zero-field and because several magnetic phases develop in an applied magnetic field [7]. Single-crystal neutron-diffraction studies in zero field [8] have corroborated these results and confirmed the earlier neutron powder-diffraction findings [6] that the magnetic phases are characterized by a transversely polarized spin-density wave with an ordering vector (wave vector) $Q \approx 0.55 a^*$ (or b^* , where a^* and b^* are reciprocal lattice vectors) and with the spins lying in the basal plane of the tetragonal crystal structure (see Fig. 1). If $Q = 0.5 a^*$ was a stable configura-

ration, the magnetic structure would consist of ferromagnetic sheets, and since the unit cell contains two Er-ions, the stacking sequence would be double layers: up-up-down-down etc. However, nesting at the Fermi surface results in phases with $Q \geq 0.55 a^*$ and introduces phase slips in the stacking of the commensurate sequences.

Recently, a mean-field model has been established and shown to account for most of the observed experimental data, including the transition from weak ferromagnetism to antiferromagnetism at 2.3 K shown in Fig. 2 [9]. The model suggests that the magnetic transitions result from a series of structures with ordering vectors $Q = n/m a^*$ (or b^*) with $0.55 \leq n/m \leq 0.60$. The present neutron-diffraction study aims to establish the modulation vectors of the stable magnetic phases and to compare the results with the predictions of the mean-field model. A detailed account of the model is published in ref. 9, and the experimental results and model analyses are presented in ref. 10.

Results and discussion

Two stable structures have been identified with ordering vector $Q = 11/20 a^*$ (or b^*) in zero field [9]. Above $T_c = 2.3$ K there is an equal number of up and down spins, but below T_c one of the spin directions becomes more populated, leading to weak ferromagnetism as visualized in Fig. 2. At low temperatures the structures are squared-up and not sinusoidal as they are close to T_N .

A field applied along $[0 1 0]$ results in the formation of two different domains. Since the spins are Ising like, the most favorable domain has $Q = n/m a^*$. When increasing the field H more up-spins are formed and phase transitions between structures with different commensurate modulation vectors result, as shown in Fig. 3a. The transverse domain stays at $Q \approx 16/29 b^* \approx 0.55 b^*$ and decreases gradually in intensity as the field is increased. The H - T -phase diagram in Fig. 3a agrees well with data derived from bulk measurements [7, 11].

When applied along $[0 0 1]$ the critical field for the antiferromagnetic phase is as high as ~ 17 T at 1.8 K. The phase diagram, studied in fields up to 12 T (the magnetic torque detached the crystal at higher fields), is shown in Fig. 3c. A gradual change of Q from $\approx 11/20$ to $\approx 5/9 a^*$ (or b^*) results when the field and/or the temperature is increased.

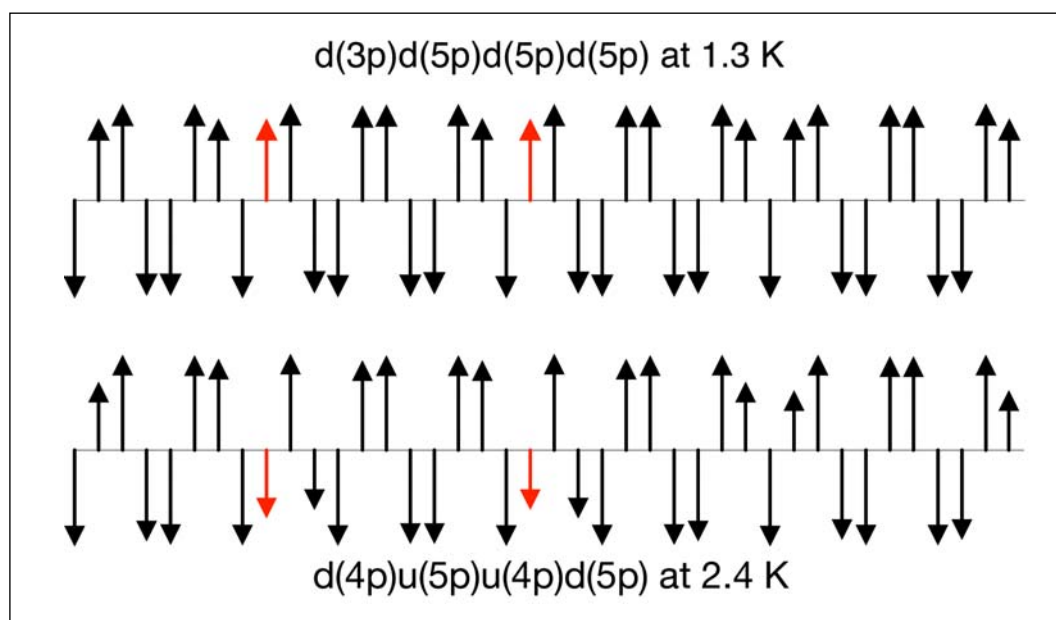


Fig. 2: One period of 40 layers of the $Q = 11/20$ zero-field structures calculated below the Curie temperature at 1.3 K, and in the antiferromagnetic phase at 2.4 K (the red arrows indicate those layers in which the moments are reversed at the transition).

Studies performed with the field along the $[1\ 1\ 0]$ direction reveal a series of ordering vectors $Q = Q_p + Q_\delta$ as a function of field and temperature. The principal ordering vector Q_p along a^* or b^* ranges from $Q_p \approx 11/20$ to $\approx 18/31$ reciprocal lattice units rlu, as shown in Fig. 3b. A peculiarity is a small, but clearly observable, rotation of the principal ordering vector Q_p by an orthogonal component $Q_\delta \approx -0.005 b^*$, which occurs close to and above the superconducting critical field, H_{c2} .

The mean-field model has been a valuable tool in the interpretation of the neutron diffraction and the bulk magnetization data. It accounts for the stability of many of the observed phases, but not for the small finite Q_δ . This small rotation shows that the exchange interaction has anisotropic components.

Acknowledgements

This work is supported by the EU Commission under contract HPRI-CT-2001-00138 on neutron-diffraction experiments at BENSC, the Danish Technical Research Council via the Framework Program on Superconductivity, and the Danish Natural Science Research Program via DANSCATT.

- [1] M.B. Maple, *Applied Physics* **9**, 173 (1976)
- [2] A.A. Abrikosov and L.P. Gorkov, *Sov. Phys. JETP* **12**, 1243 (1961).
- [3] M.B. Maple and O. Fischer (edt.): *Superconductivity in Ternary Compounds, Topics in Current Physics*, Vols. I and II, (Springer, Berlin, 1982).
- [4] R. Nagarajan et al. *Phys. Rev. Lett.* **72**, 274 (1994).
- [5] R.J. Cava et al. *Nature* **367**, 254 (1994).
- [6] J.W. Lynn et al. *Phys. Rev. B* **55**, 6584 (1997).
- [7] P.C. Canfield et al., *Physica C* **262B**, 249 (1996).
- [8] S.-M. Choi et al., *Phys. Rev. Lett.* **87**, 107001 (2001).
- [9] J. Jensen, *Phys. Rev. B* **65**, 140514 (2002).
- [10] A. Jensen et al., *Phys. Rev. B* **69**, 104527 (2004).
- [11] S.L. Budko and P.C. Canfield, *Phys. Rev. B* **61**, R14932 (2000).

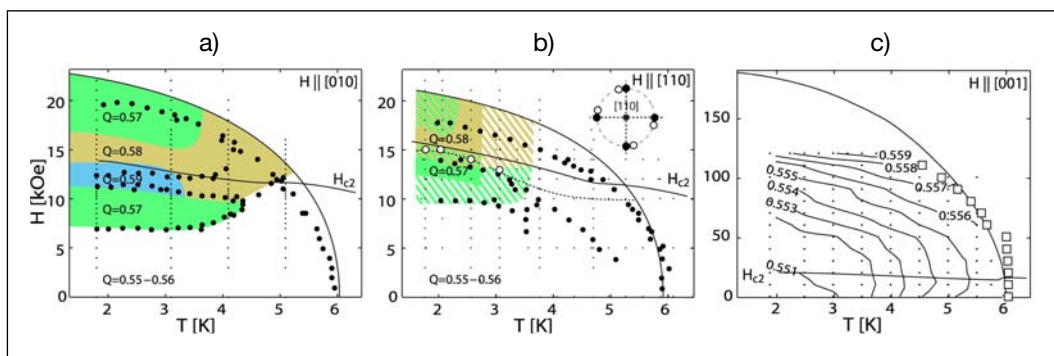


Fig. 3: Magnetic phase diagrams of ErNi₂B₂C for the magnetic field applied along a) $[0\ 1\ 0]$, b) $[1\ 1\ 0]$ and c) $[0\ 0\ 1]$. Small black dots mark the (T, H) points where the magnetic intensity disappears. In c) the boundary lines in a) and b) interpolate points where the magnetic intensity disappears. In c) the boundary line is the Néel temperature determined by the mean-field model. A fine solid line marks the superconducting critical field H_{c2} , and the solid circles indicate the magnetic phase lines derived from magnetization measurements [11]. Four commensurate phases are presented in the phase diagram a) with $H \parallel [0\ 1\ 0]$. In b), $H \parallel [1\ 1\ 0]$, coloured areas indicate the existence of one of the three phases, and the striped areas represent coexistence of two phases. The modulation vector has a finite transverse component above the dashed line, and the open circles indicate that the orthogonal component is zero at lower field. The insert shows schematically how the magnetic reflections are rotated in reciprocal space. In c), with $H \parallel [0\ 0\ 1]$, the contours indicate that Q increases continuously as function of H and T ; the open squares represent the Néel temperature derived from the data.

Boundary Layers of Water at Polymer-Liquid Interfaces

R. Steitz, S. Schemmel, G.H. Findenegg

■ Technische Universität Berlin

Interfaces of hydrophobic substrates against aqueous media are of broad interest in view of their ubiquitous presence in biological and other types of colloidal systems. It is generally believed that the adsorption of apolar molecules from aqueous solutions onto a hydrophobic surface, like their aggregation in water, is caused by hydrophobic interactions [1]. Recent theoretical studies [2] have indicated, however, that the nature of the solvation of small and large apolar species in water is quite different: Hydrogen bonding of water persists around small molecules but is depleted near large species, leading to a drying phenomenon, i.e. a drastic reduction of the local density of water near the surface of large species, which is absent for species of radius less than ca. 1 nm. Modern techniques like X-ray and neutron reflectometry are ideally suited to experimentally cross check above predictions on extended systems. The fraction of reflected X-rays or neutrons is a direct measure of the density profile across the interface on the molecular scale. Neutron reflectometry (NR) is particularly useful as it offers the possibility to enhance the sensitivity by changing the scattering contrast, mostly by replacing weak scattering protons (^1H) by strong scattering deuterons ($^2\text{H} = \text{D}$) without distorting the chemical nature of the system under investigation.

Neutron reflectivity experiments on the interface of deuterated polystyrene films (d-PS) and heavy water (D_2O) revealed that water is depleted (to ca. 90 % bulk water density) in a ca. 3 nm thick boundary layer of the liquid phase against the hydrophobic substrate [3]. This finding coincides with reports on two similar systems [4, 5] where water depletion layers were also observed. All findings can be explained in the general context of wetting (or non-wetting) and in particular in the context of above mentioned theory of a drying transition [2] where the depletion of water is seen as a (weak) dewetting of the hydrophobic walls (d-PS coating, alkane monolayer) in contact with the bulk aqueous phase [6].

On a macroscopic scale, the wetting behaviour is characterized by the contact angle of the liquid at the surface of the substrate. Commonly, the ad-

vancing contact angle of macroscopic droplets of water, ϑ , is taken as a measure of the hydrophobicity (and wettability) of surfaces (see Fig. 1):

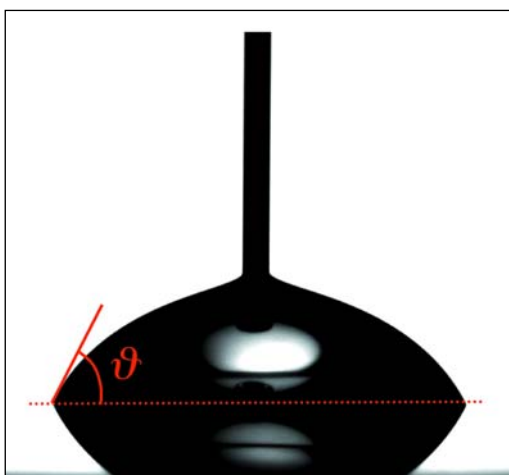


Fig. 1: Image of a water droplet (diameter ca. 3 mm) on a polymer substrate at which the contact angle ϑ at the three-phase contact line (substrate/ liquid/ vapor) is less than 90° . This is a signature of a weakly hydrophobic or hydrophilic substrate.

Contact angles $\vartheta > 90^\circ$ indicate hydrophobic surfaces, while $\vartheta < 90^\circ$ indicate weakly hydrophobic or hydrophilic surfaces.

For water on d-PS coatings, $\vartheta = 90^\circ$, and thus it is not unexpected to find that water is depleted in the boundary layer against d-PS surfaces. It is more of a surprise that water is also depleted near ethyleneoxide-terminated self-assembled monolayers (EG3-OMe SAMs), for which the water contact angle is only 63° [5]. Furthermore, measurements of force as a function of distance between two organic surfaces immersed in aqueous solutions, performed by Ishida et al. [7], indicated the onset of hydrophobic interactions at even lower water contact angles ($\vartheta \approx 40^\circ$). This observation is remarkable as the onset of hydrophobic interactions is an indicator for incipient drying of the surfaces.

Contact angles in the range of 30–70° are also typical for water or aqueous solutions at poly-electrolyte coatings. In the present work we prepared multilayer films, Si/PEI/(d-PSS/PAH)₆ ($\vartheta = 63^\circ$) and Si/PEI/(d-PSS/PAH)₆/d-PSS ($\vartheta = 37^\circ$), from the respective polyelectrolytes PEI (polyethylene-imine), d-PSS (deuterated polystyrene sulfonate) and PAH (poly-allyl-hydrochloride), by “layer-by-layer” deposition [8] on top of silicon single crystals. The polyelectrolyte-coated silicon single crystals served as the top of a flow cell made up by a Teflon trough (see Fig. 2).

Polyelectrolyte multilayers absorb substantial amounts of water [9]. The scattering length density, Nb, of the films and of the water phase can be matched by using appropriate mixtures of D₂O and H₂O, and in this way the film/water interface should become invisible to the impinging neutrons in the absence of a depletion layer. Thus, polyelectrolyte coatings are ideal model systems to check the relation between water contact angle and the appearance of water depletion by neutron reflectometry.

Fig. 2 shows reflectivity curves for a given polyelectrolyte coating (ca. 30 nm thickness) against pure D₂O, pure H₂O and a contrast-matching D₂O/H₂O mixture. From these and further results for a series of different D₂O/H₂O mixtures the scattering length density (sl) of the polyelectrolyte film at given D₂O/H₂O compositions of the water phase was extracted from fits to the spectra (solid lines in Fig. 2, bottom) and plotted versus the scattering length density of the water phase. By this procedure the matchpoint of polyelectrolyte film and bulk water phase was found to be $5.03 \cdot 10^{-6} \text{ \AA}^{-2}$. For this condition the Kiessig fringes stemming from the interference of neutrons that are reflected at the silicon/film and at the film/water interface, respectively, are completely suppressed (Fig. 2 bottom left, middle curve). This finding proves that the polyelectrolyte coatings are indeed contrast matched, but it also indicates that there is no significant depletion of water at the hydrophilic polyelectrolyte/water interface. At least it is safe to say that water depletion is much less pronounced than observed at the hydrophobic d-PS/water interface. The same conclusion also holds for the d-PSS terminated films.

Interestingly, the contact angle of water on the PAH-terminated polyelectrolyte multilayers is almost the same as on the EG3-OMe terminated SAMs of reference [5]. Nevertheless, the wetting behavior of these two surfaces appears to be quite different. While the water-sorbing polyelectrolyte coatings do not induce a depletion layer of water, pronounced depletion of water is found at

the non-swelling SAMs. This demonstrates that the water contact angle cannot be taken as an unambiguous indicator of the onset of the drying transition of water at hydrophobic surfaces. Apparently our knowledge about interfaces that are generally considered “simple” is far from complete.

- [1] Israelachvili, J., *Intermolecular and Surface Forces*, 2nd Ed., Academic Press: London, UK, 1992, p. 128 ff.
- [2] Lum et al., *J. Phys. Chem. B*, **103**, 4570 (1999).
- [3] Steitz et al., *Langmuir*, **19**, 2409 (2003)
- [4] Torben et al., *Phys. Rev. Lett.* **90**, 086101 (2003).
- [5] Schwendel et al., *Langmuir*, **19**, 2284 (2003).
- [6] Ball, *Nature*, **423**, 25 (2003).
- [7] Ishida et al., *J. Coll Interface Sci*, **216**, 387 (1999).
- [8] G. Decher, *Science* **277**, 1232 (1997).
- [9] Steitz et al., *Colloid Surfaces A*, **163**, 63 (2000).

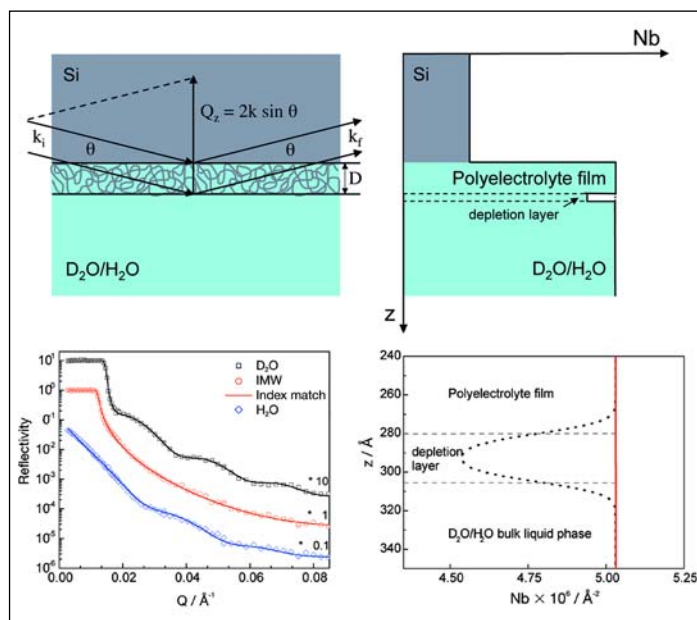


Fig. 2: Scattering geometry (top left), schematic scattering length density profiles (top right), reflectivity curves (bottom left) and zoom-in on the scattering length density profile at the polymer/water interface (bottom right). Note that the polymer film sandwiched between the silicon backing and the water fronting is invisible to the incident neutron beam upon appropriate index-matching of the liquid phase (red solid lines, bottom left and right). In this case the neutrons are reflected from the silicon/polymer interface only and thus the characteristic oscillations of the reflectivity curve are lost. The black dotted line shows the profile of the scattering length density across the polymer/liquid interface. For details see text.

Neutron Autoradiography of the painting *Armida abducts the sleeping Rinaldo* (~1637) by Nicolas Poussin

C. Laurenze-Landsberg¹, C. Schmidt¹, L.A. Mertens², B. Schröder-Smeibidl²

■ 1 Berlin Picture Gallery (Gemäldegalerie Berlin) ■ 2 HMI



Fig. 1: Nicolas Poussin, Replica, *Armida abducts the sleeping Rinaldo*, (c. 1637), Berlin Picture Gallery, 120 × 150 cm², Cat No. 486

analysis of materials and techniques used in painting. It allows the visualization of structures and layers under the visible surface and, in addition, enables one to identify in detail the elements contained in the pigments. The instrument B8 at the Berlin Neutron Scattering Center BENSC is dedicated to these investigations.

Isotope	Half life	Pigment
⁵⁶ Mn	2.6 h	Brown colours, Umber, Ocre
⁶⁴ Cu	13 h	Azurite, Malachite
⁷⁶ As	1.1 d	Smalt, Realgar, Auri-pigmente
¹²² Sb	2.7 d	Naples-Yellow
¹²⁴ Sb	60 d	
³² P	14 d	Bone-black
²⁰³ Hg	47 d	Vermillion
⁶⁰ Co	5.3 a	Smalt

Table 1: Main isotopes and pigments used in neutron autoradiography and their half-lives

In close collaboration, the Berlin Picture Gallery (Gemäldegalerie Berlin, Stiftung Preussischer Kulturbesitz) and the Hahn-Meitner Institute investigate old masters paintings by means of neutron autoradiography. Neutron

autoradiography is a very effective, non-destructive, but rather exceptional method applied in the examination and

Neutron autoradiography – the method and the instrument

Usually, when examining paintings, museums apply methods based upon the use of photon radiation. However, the information provided by these methods is limited. Infrared reflectography reveals black carbon-based media, whilst X-ray transmission-records

only indicate the distribution of heavy elements like iron or lead, e.g. in the pigment lead-white. As a complementary method, neutron autoradiography is capable of revealing different paint layers piled-up during the creation of the painting. In many cases, the individual brushstroke applied by the artist is made visible as well as changes and corrections introduced during the painting process. By using paintings that have been reliably authenticated, one can identify the unique style or “hand” of a particular artist.

The experimental principle

The experimental principle is simple: In the first step, the painting is irradiated at the instrument B8 by neutrons from the research reactor BER II. Some of the atomic nuclei within the painting capture one of the neutrons thus becoming radioactive. The probability of capture depends on the activation cross-section specific for every isotope. During the irradiation, the painting is fixed on a support in front of the neutron guide end (open area: 3.5 × 12.5 cm²). The surface of the painting is adjusted under a small angle (< 5°) with respect to the axis of the guide. This way, the main free path of the neutrons within the paint layer becomes much longer than in the case of perpendicular transmission. The support is then moved up and down with a velocity of a few cm/s allowing for a uniform activation of the total area of the panel. Due to the short irradiation time, only 4 of 10¹² atoms became radioactive on average, insofar the method is considered as a non-destructive investigation. After irradiation, the neutron-induced radioactivity decays with time. Around a dozen of different light and heavy isotopes – emitting β- (electrons) and γ-radiation – are created. The most important isotopes, their half-lives and the corresponding pigments are presented in Table 1. The induced β-decay blackens highly sensitive films or imaging plates thus unveiling the spatial distribution of the pigments. The big advantage of neutrons lies in the fact that different pigments can be represented on separate films. This is due to a con-

trast variation created by the differences in the half-lives of the isotopes. The γ -spectroscopy provides information about the element composition in the pigments. The image plate technique allows for direct digital analysis and processing.

The investigation of the painting *Armida abducts the sleeping Rinaldo* (c. ~1637) by Nicolas Poussin

Nicolas Poussin (1594–1665), one of the main representatives of pictorial classicism in the Baroque period, was French, but spent his entire career in Rome with the exception of two years as court painter to Louis XIII. The illustrations in his paintings address scenes from the Bible and from classical antiquity. Already in 1625, the legend of the sorceress Armida and the crusader Rinaldo had inspired Poussin to a painting named *Armida and Rinaldo*, now owned by the Dulwich Picture Gallery in London, that is accepted as being an original. In contrast, the painting at the Berlin Picture Gallery *Armida abducts the sleeping Rinaldo* (Fig. 1) showing a different but similar scene, is up to now listed in the Berlin Gallery's catalogue as a copy.

To clarify the open question of the ascription, an investigation by means of neutron radiography was carried out at the Hahn-Meitner Institute. The record of an X-ray radiography (Fig. 2) applied as a complementary method did not contribute to the solution of the problem revealing primarily the image of the wooden frame. Because of the size of the painting, the neutron radiography had to be carried out in two separated irradiations. In Fig. 3, one of the autoradiographs is depicted. The different sets of image plates were processed digitally and assembled afterwards. Already this first record, showing the distribution of the short-lived isotope ^{56}Mn contained in the brown pigment umber, reveals surprising conceptual changes – so called *pentimenti*: additional trees (highlighted in Fig. 3) not present in the final painting. Obviously, these *pentimenti* are corrections made by the master himself. A copyist would not have been aware of these changes. Therefore, these *pentimenti* are strong and important hints that this painting can possibly be ascribed to Nicolas Poussin himself.

Summary

With neutron autoradiography painting techniques or conceptual changes and corrections of a painting become visible. The art historian or the restorer obtains valuable information about the artist's brushstroke and the actual condition of the painting. In some cases, decisions about the authenticity can be made. In addition, this method is used more and more as an instrument supporting the restoration of paintings. The example presented above impressively demonstrates the efficiency of neutron autoradiography as a method for the examination of paintings.

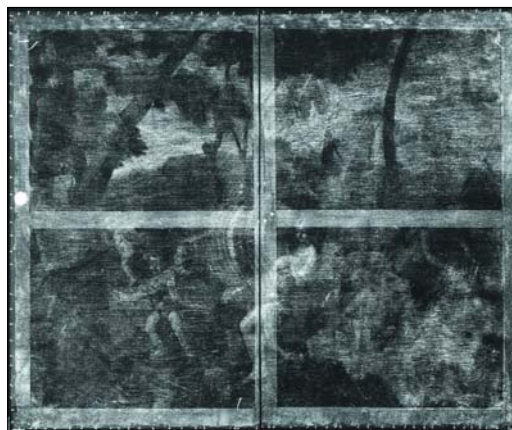


Fig. 2: Nicolas Poussin, Replica, *Armida abducts the sleeping Rinaldo*, X-Ray transmission record, Picture Gallery Berlin

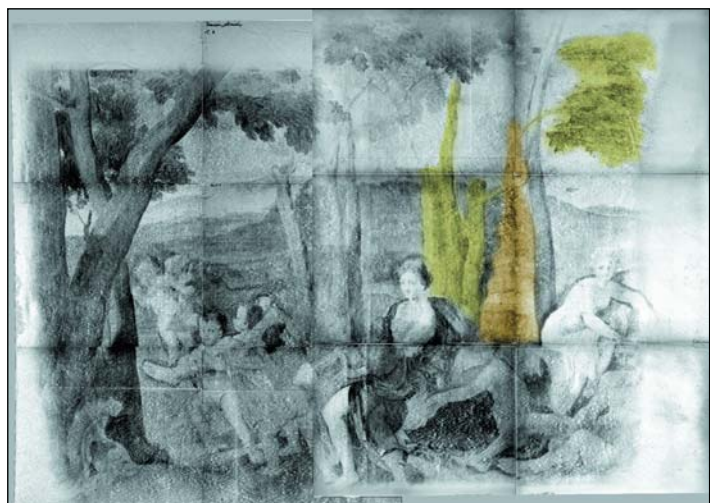


Fig. 3: Nicolas Poussin, Replica, *Armida abducts the sleeping Rinaldo*, 1st neutron autoradiography assembled from 12 image plate records: In order to investigate the whole picture, two separated irradiations were carried out and finally recomposed.

Plastic deformation of amorphous silicon under swift heavy ion irradiation

A. Hedler¹, W. Wesch¹; S. Klaumünzer²

■ 1 Friedrich-Schiller University, Jena ■ 2 HMI, SF4

All investigated amorphous materials show anisotropic plastic deformation under swift heavy ion irradiation (SHI) as a consequence of multiple anisotropic high electronic energy deposition referred to as ion hammering [1–3]. In the past years this effect has been discussed controversially [4–7]. The viscoelastic thermal spike theory by Trinkaus et al. [4, 5] represents a good description for glasses which show a continuous transition to the liquid state. However, a verification of the model for amorphous semiconductors, which show a phase transition of first order, has not been undertaken. With its well-known physical properties amorphous Si (a-Si) seems to be a suitable candidate to be investigated first.

Single-crystalline, 370 μm thick, one-side polished Si wafers were amorphized by means of multiple Si implantation at 77 K with energies of 0.25–9.5 MeV and ion fluences of $3\text{--}7 \cdot 10^{15} \text{ cm}^{-2}$ at the Tandatron accelerator of FSU Jena. Rutherford-backscattering spectrometry, infrared-reflection spectrometry and cross-sectional transmission electron microscopy imaging revealed a homogenous amorphous surface layer with a thickness of $d = 5.7 \mu\text{m}$. In order to measure surface shifts with a precision of 1 μm an Au grid layer of 40 nm thickness has been produced on the sample surface by subsequent Au evaporation through a Ni net.

Swift heavy ion irradiation of the samples was carried out at HMI with the conditions described in Table 1.

Ion/Energy	Θ	T_0 [K]	S_e [keV/nm]
390 MeV Xe ²¹⁺	45°	77, 300	15.8 \pm 0.2
350 MeV Au ²⁶⁺	45°	77, 300	18.8 \pm 1.0
600 MeV Au ³⁰⁺	45°	77, 300	21.3 \pm 0.3

Table 1: Irradiation conditions: the angle of the ion beam with respect to the surface normal Θ , the irradiation temperature T_0 and the mean value of the electronic energy deposition in the a-Si layer S_e as calculated by SRIM-2003.

By mounting the sample on a holder with a movable aperture micrographs of the transition region between irradiated and unirradiated surface parts were taken in-situ with a long-distance microscope. As an example, Fig. 1 shows a micrograph of the surface shift of a sample irradiated with electronic energy deposition $S_e = 18.8 \text{ keV/nm}$ at $T_0 = 77 \text{ K}$ indicating the occurrence of plastic flow of a-Si under SHI.

In order to quantify the plastic flow process, the dependence of the surface shift Δx on the ion fluence Φt has been measured for each SHI condition. Fig. 2 shows the results for the irradiations at $T_0 = 77 \text{ K}$.

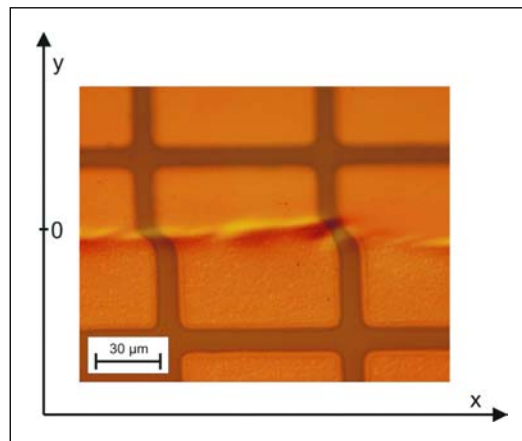


Fig. 1: Micrograph of a calibrated a-Si sample. The grid distance is 85 μm . The upper part ($y \geq 0$) has not been irradiated, the lower part ($y \leq 0$) has been irradiated at $T_0 = 77 \text{ K}$ with 350 MeV Au and an ion fluence of $\Phi t = 1.65 \cdot 10^{15} \text{ cm}^{-2}$ under an angle of $\Theta = 45^\circ$ from left.

A linear dependence of $\Delta x(\Phi t)$ and an intensified plastic flow with increasing S_e have been observed. For room-temperature irradiation and small fluences the data points lie slightly below those in Fig. 2. The linear increase of $\Delta x(\Phi t)$ is a well-known feature of the ion hammering

effect of embedded amorphous layers within crystalline surroundings and can be understood with the extended Maxwell model [1–3]

$$\dot{\underline{\epsilon}} = \underline{A} \cdot \Phi + \dot{\underline{\epsilon}}_{\text{elast}} + \dot{\underline{\epsilon}}_{\text{visc}} \quad (1)$$

which describes the macroscopic deformation $\underline{\epsilon}$ as a superposition of the ion hammering effect, characterized by the deformation yield tensor \underline{A} , with the elastic and viscous properties of the layer, characterized by $\underline{\epsilon}_{\text{elast}}$ and $\underline{\epsilon}_{\text{visc}}$, respectively. In case of quasi-static equilibrium and stress-free surfaces this model has a solution far from the interfaces, which describes the surface shift as a function of the ion fluence

$$\Delta x = 3A_0 d \cdot \sin 2\Theta \cdot \Phi t. \quad (2)$$

The tensor \underline{A} reduces to the scalar A_0 denoted as deformation yield per ion and determines the slope of the linear dependence $\Delta x(\Phi t)$ and thus the strength of the anisotropic growth. Trinkaus et al. assigned A_0 to the ion-solid-interaction and could derive an expression for the dependence of A_0 on both the irradiation condition (energy deposition, irradiation temperature) and the target material properties [4–5].

Being aware of the layer thickness d and the incident angle of the ions Θ the dependence of the deformation yield A_0 on the electronic energy deposition S_e can be calculated for both irradiation temperatures by using Eq. (2). The results are shown in Fig. 3. As a rough approximation a linear dependence of $A_0(S_e)$ has been observed for both irradiation temperatures. For constant energy deposition A_0 decreases with increasing T_0 due to enhanced stress relaxation in the surroundings of the ion path [4-5] resulting in a lower slope dA_0/dS_e for the higher T_0 . The energy deposition threshold of the plastic deformation can be assigned to $S_{e0} = 14.2$ keV/nm and is independent of the irradiation temperature. The observed value of the normalized deformation yield for $T_0 = 77$ K $dA_0/dS_e = 4.6 \cdot 10^{-14} \text{ m}^3/\text{J}$ is an order of magnitude lower than typical values for metallic glasses [4-5] and is obviously due to the first order phase transition occurring during the thermal spike phase in a-Si.

Further investigations should be directed to a possible explanation of the observed normalized deformation yield at the low irradiation temperature with an extended Trinkaus theory including the phase transition of first order in a-Si.

- [1] S. Klaumünzer, Multisc. Phenom. in Plasticity, 441 (2000).
- [2] A. Gutzmann, S. Klaumünzer, P. Meier, Phys. Rev. Lett. **74**, 2256 (1995).
- [3] A. Gutzmann, S. Klaumünzer, Nucl. Instr. & Meth. B **127/128**, 12 (1997).
- [4] H. Trinkaus, A.I. Ryazanov, Phys. Rev. Lett. **74**, 5072 (1995).
- [5] H. Trinkaus, J. Nucl. Mater. **223**, 196 (1995).
- [6] L. Cliche, S. Roorda, M. Chicoine, R.A. Masut, Phys.Rev.Lett. **75**, 2348 (1995).
- [7] M. Chicoine, S. Roorda, L. Cliche, R.A. Masut, Phys. Rev. B **56**, 1551 (1997).

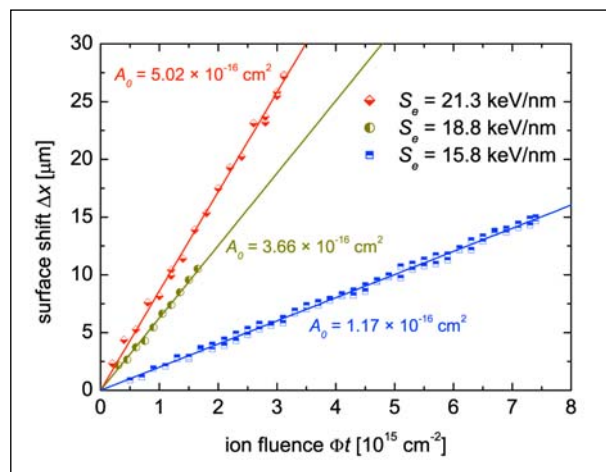


Fig 2: Dependence of the surface shift Δx on the ion fluence Φt for the irradiations at $T_0 = 77$ K.

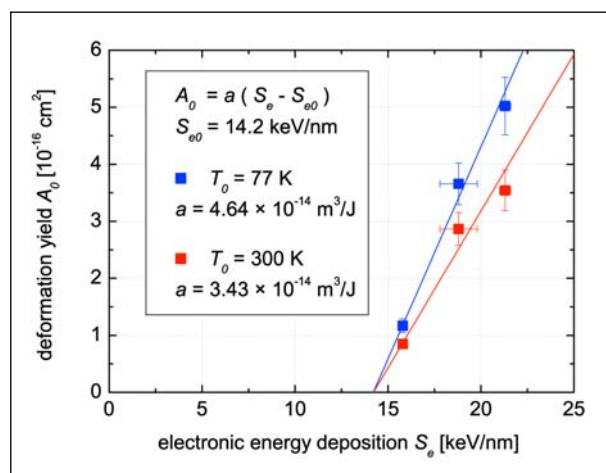


Fig. 3: Dependence of the deformation yield per ion A_0 on the electronic energy deposition S_e . The threshold value of S_e is denoted as S_{e0} .

Surface modification by irradiation with swift heavy ions

W. Bolse¹, B. Schattat¹, H. Paulus¹, I. Zizak², N. Darowski², S. Klaumünzer²

■ 1 Institut für Strahlenphysik, Universität Stuttgart ■ 2 HMI, SF4

Swift heavy ions at energies of the order of MeV/amu are slowed down in a solid predominantly by electronic excitation and ionization of the target atoms, while nuclear energy deposition by elastic collisions is negligible. Defect creation and amorphous track formation due to electronic energy deposition, which has been observed especially in insulators, demonstrate that part of the electronic excitation energy is transferred to the lattice. In thin film packages, swift heavy ion irradiation results in atomic mixing at the interfaces. In former experiments it was shown that interface mixing in oxide bilayers occurs as soon as a certain threshold S_{ec} is exceeded, which is given by track formation threshold of the less sensitive material of the bilayer [1, 2]. The threshold for interface mixing of NiO/SiO₂ is given by NiO, where we have investigated the track formation, too.

Samples and irradiation

NiO single crystals prepared for transmission electron microscopy (TEM), as well as NiO bulk material and the thin layer system NiO/SiO₂ have been irradiated with 90 MeV to 350 MeV Ar, Kr, Xe and Au ions at $T = 80$ K and low fluences, ($\sim 10^{10}$ cm⁻²), where the single ion impacts are clearly separated from each other.

The irradiations were performed at Hahn-Meitner Institute, Berlin. No tracks were observed after irradiation with 90 MeV Ar ions, while discontinuous track fragments became visible after irradiation with 140 MeV Kr ions. This is in good agreement with the intermixing and self organization behaviour in NiO/SiO₂-bilayers, where the effects could only be observed after irradiation with ions heavier than Ar [3]. Continuous tracks, with their number density being in agreement with the ion fluence, were formed during irradiation with 230 MeV Xe and 350 MeV Au, respectively.

In Fig. 1, the top view of a NiO-sample irradiated with 350 MeV Au is shown, while in Fig. 2 the sample was tilted by 40°, displaying continuous tracks. Furthermore, spherical nanoparticles have been formed at the ends of these tracks. Fresnel contrasts, which evidence voids, were observed along the tracks and prove that the center of the tracks is empty. The void formation conforms with the nanoparticle formation at the surface. Similar nanoparticles have been observed at the top of NiO/SiO₂ due to swift heavy ion irradiation with low fluences.

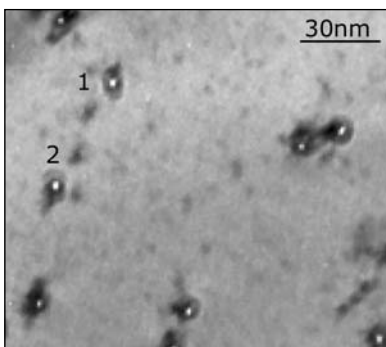


Fig. 1: TEM image of the single NiO crystal irradiated with $4 \cdot 10^{10}$ cm⁻² 350 MeV Au. The image was taken normal to the surface.

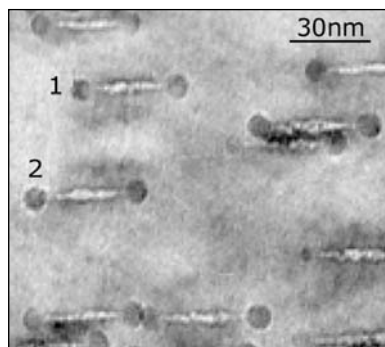


Fig. 2: Same position on the same sample as in the Fig. 1. Sample was tilted 40° for the TEM. Note the corresponding tracks marked with numbers in the figures 1 and 2. The irradiation led to the creation of hollow tracks with small spheres at the ends.

Experiment

X-ray scattering methods have been proven to be a powerful tool for non-destructive analysis of the shape, size distribution and density fluctuations of solid state matter. Using the 6-circle goniometer at the KMC2 beamline at BESSY and the available area sensitive detector, it was possible to study the diffuse small angle scattering (SAXS), recording the beam reflected from the sample surface (GISAXS). This geometry allows one to gain information about structures at the surface with a size of a few nanometers, and is therefore well-suited for the investigation of the pellets on the irradiated NiO-samples. The shape of the pellets, their size distribution and parts of the ion track near the surface can be studied and characterized.

The goniometer at the KMC2 beamline is optimized for surface investigations using the grazing incidence angle geometries, and, in combination with the well collimated beam and the area sensitive detector, it is suitable for GISAXS measurements.

After the sample surface was aligned with the incident beam, fast qualitative reflectometry measurements were performed to estimate the angle of total reflection for the specific sample. Changing the incident angle in the GISAXS experiment allows the study of different depths under the surface. If the GISAXS measurement is performed with incident angle smaller than the total reflection angle, only objects which are above the surface are detected. If the incident angle is larger, part of the photons is penetrating the surface and being scattered on the objects below the surface. This way, the scattering of the pellets and the hollow tracks can be measured separately.

Results and Discussion

Since only one half of each sample was irradiated, we were able to measure the scattering from the unirradiated part, and use these measurements for the background correction.

Fig. 3 shows the detected scattered intensity from the thin NiO/SiO₂ irradiated with $5 \cdot 10^{10}$ 350 MeV Au ions/cm². The resolution and the signal to noise ratio were not very satisfactory, so only a part of the planned evaluation was performed. The scattering pattern measured on the unirradiated part of the sample was subtracted from the pattern measured on the irradiated part. The resulting scattering pattern was fitted with the model function of mono-disperse spheres laying on the sample surface to obtain the radius of the pellets. The resulting radius of the pellets was 6.2 nm. Thick NiO single crystals showed no difference in scattering function between the irradiated and the unirradiated part.

Although GISAXS offers more information on the surface objects, it was not possible to evaluate the measured data with the expected success. Low intensity of the primary beam and large noise made the detection of the hollow tracks impossible. However, we were able to detect and estimate the size of the spheres on the surface of some irradiated samples. This experiment showed that GISAXS provides information on irradiated samples which are very hard to measure with other methods.

In 2005, a new SAXS experimental station is going to become operational at the 7 T wiggler at BESSY. The new station is optimized for the surface scattering, and we plan to continue this experiment at the new device. We hope to be able to measure not only the radius of the spheres, but also the radius and the dimensions of the hollow track.

-
- [1] W. Bolse, B. Schattat, Nucl. Instr. Meth. B **190**, 173 (2002).
 - [2] B. Schattat, W. Bolse, S. Klaumünzer, F. Habsmeier, A. Jasenek, Appl. Phys. A **76**, 165 (2002).
 - [3] W. Bolse, B. Schattat, A. Feyh, Appl. Phys. A **77**, 11 (2003).

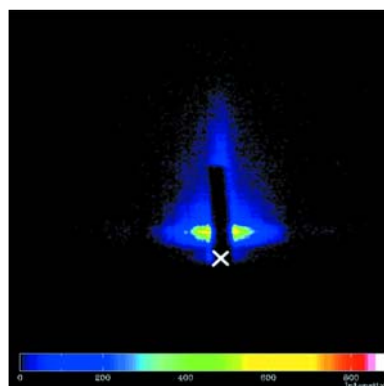


Fig. 3: Enlarged image from 2d area detector. The white cross marks the position of the primary X-ray beam. The sample surface is parallel to the x -axis of the detector, and the photons are reflected upwards. The dark box in the middle is the shadow of the beam stopper, which protects the detector from the directly reflected beam. The scattering in the surface direction can be seen left and right from the reflected beam.

Tendaguru Sauropod Dinosaurs – Characterization of Diagenetic Alterations in Fossil Bone

M. Stempniewicz, A. Pyzalla

■ Institut für Werkstoffkunde und Materialprüfung, Technische Universität Wien, Austria

Sauropod dinosaurs, and more specifically *Barosaurus africanus* and *Brachiosaurus brancai*, were animals of tremendous size. The physiological and biochemical consequences of this size and the resulting weight estimated to reach up to 100 t [1] makes these dinosaurs subject of our interest. In the project presented here we investigate the structure of the animals' fossilized bones – a study exclusively based on the fossil record, i.e. the excavated skeletons.

In fossilized sauropod bone significant structural changes may have occurred due to the interdiffusion between the bone and the environment it was buried in for about 150 million years. In order to assess these diagenetic changes (alterations to a material's original mineralogy and texture due to geological processes), the chemical composition of several fossilized bones from the Tendaguru dinosaur bed (Tanzania, East Africa) is studied. These bones were excavated during the Tendaguru Expedition run by Janensch in the years 1909–1913 [2] and have been stored at the Museum of Natural History of the Humboldt-University in Berlin (NHUB). Cores were taken from the middle shafts of femora and humeri of the sauropod skeletons by PD Dr. M. Sander, University of Bonn. We investigated the cores, i.e. cross-sections through the middle shafts, in order to determine their structure on different hierarchical levels as well as their texture (orientation distribution of the crystallites). Since material from individuals belonging to the same species, yet buried in different stages of ontogenetical development, is available, we expect that the growth process of the sauropods can be studied.

For the assessment of diagenetic changes in the sample material quantitative analyses of their elemental composition were necessary. The measurements were performed at the ISL-cyclotron by means of the PIXE method (Proton Induced X-Ray Emission). All experiments were carried out in air with a 68 MeV proton beam with an area of $(2 \times 2) \text{ mm}^2$. The cross sections obtained from the cores were scanned radially from the periosteal surface (outer surface of the bone) to the border of the trabecular ("spongy") bone at the endosteal surface (inside surface of bones that borders the bone marrow cavity). The characteristic X-rays emitted from the targets were collected by an HPGe-detector. From the obtained spectra quantitative analyses were performed.

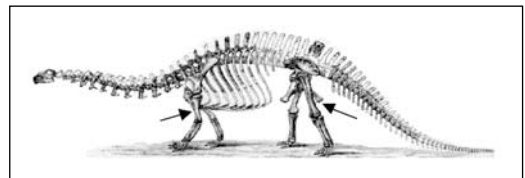


Fig. 1: General built of a sauropod dinosaur with indicated humerus and femur bones (arrows).

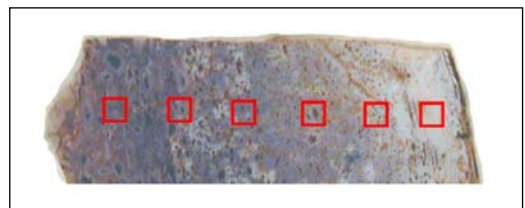


Fig. 2: Radial cut of a cross section of a femoral shaft of the *Barosaurus africanus* individual with indicated measurement points. Spot size: $2 \times 2 \text{ mm}^2$.

Fig. 2 shows a typical radial cut of a cross section with measurement points located on it. Concentration profiles from all samples are similar (Fig. 4). Among the observed element distributions those of manganese, strontium and uranium are the most interesting. Though the bones remained buried for 150 million years, the elements are still not evenly distributed. Uranium and strontium concentrations differ in absolute concentrations, but they seem to follow the same pattern. Strontium, that exchanges calcium in the apatite structure, shows relatively higher concentrations toward the outer surface. Manganese, in turn, is present only inside the bone (in the pores), its concentration increases toward the inner part of the bone. The absence of manganese in the cortex indicates that only minor diagenetic alterations of the bone occurred, since this element was not incorporated in the biological processes during the lifetime of the sauropods. Iron is enriched in certain areas and causes the typical brownish tint. There are several biological and geochemical processes that might explain these observations.

In our previous studies of the Tendaguru skeletons, we determined the crystallographic structure of the bone mineral, its habit and density [3]. In addition, the application of PIXE yielded concentrations of various elements and their distribution over the sample. From the results we conclude that some chemical alterations occurred (strontium incorporation into bone mineral) but they were not very significant since manganese is only present in the pores and does not infiltrate the bone cortex. Therefore, the bone mineral particles are not fully recrystallized and further analyses of the crystallites can be interpreted in contexts of an individual's life history. More details may be found in [4].

The authors gratefully acknowledge Dr. Andrea Denker from ISL for her invaluable help during and after experiments.

- [1] J. Peczkis, *Implications of body mass estimates for dinosaurs*; *Journal of Vertebrate Paleontology* **14**, 520–533 (1994).
- [2] W-D. Heinrich, *The Taphonomy of Dinosaurs from the Upper Jurassic of Tendaguru (Tanzania) Based on Field Sketches of the German Tendaguru Expedition (1909–1913)*, Mitt. Mus. Nat. kd. Berl., Geowiss. **2**, 25–61 (1999).
- [3] M. Stempniewicz, B. Camin, A. Pyzalla, *Preliminary Investigation of Fossil Bone: XRD and XPS study*, Proceedings of the 13th Conference of European Society of Biomechanics, Acta of Bioengineering and Biomechanics, 4 (2002) Suppl.1.
- [4] M. Stempniewicz, A. Pyzalla, M. Sander, P. Hinkel, S. Weiss, A. Denker: *Microscopical and PIXE Studies of Giant Sauropod Bones*, in preparation.

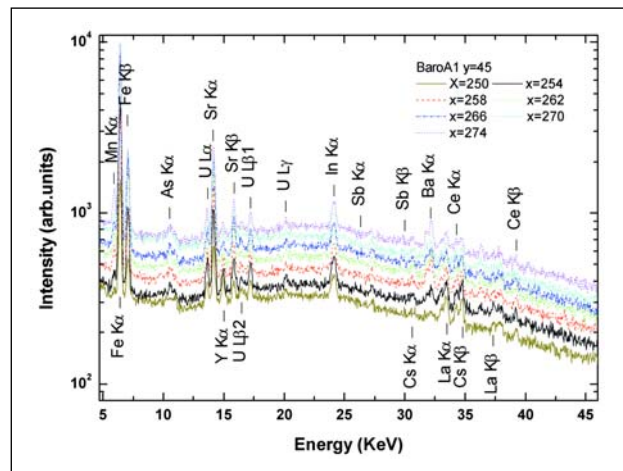


Fig. 3: PIXE spectrum recorded on different points of one section (*Barosaurus africanus* femur).

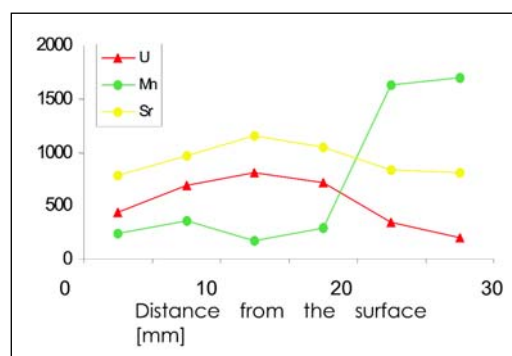


Fig. 4: Representative elemental distributions obtained by scanning a radial cut of a cross section (*Barosaurus africanus* femur).

Fluid and particle retention in the hippos Kathi and Josef of the Berlin Zoo investigated by Neutron Activation Analysis

A. Schwarm², S. Ortmann², M. Clauss³, D. Alber¹, D. Behne¹

■ 1 HMI, SF6 ■ 2 Institute of Zoo and Wildlife Research (IZW), Berlin ■ 3 Institute of Animal Physiology and Animal Nutrition, Oberschleissheim, Germany

There are two basic forms of digestive systems among herbivorous mammals: In foregut fermenters such as ruminants (i.e. cow, sheep, goat) and other non-ruminating mammals with forestomachs (i.e. hippo, kangaroo) the fermentation of the food by microorganisms proceeds the enzymatic digestion while in hindgut fermenters (i.e. horse, rhino, rabbit) it is the other way round. In most hindgut-fermenting mammals, larger particles are preferentially excreted as they are more difficult to digest and their retention would limit further food intake. In ruminants which submit retained larger particles to repeated chewing, has selective large particle retention been considered to be advantageous. It has been assumed that other mammalian herbivores with forestomachs have a particle retention mechanism similar to that of ruminants, but this has not yet been investigated.

In order to obtain first information on this matter, the particle retention was investigated in one animal each of two non-ruminant mammalian foregut fermenters, the Common hippopotamus (*Hippopotamus amphibious*, Kathi) and the Pygmy hippopotamus (*Hexaprotodon liberiensis*, Josef) kept at the Berlin Zoo. The study was carried out by means of an elemental tracer technique. Hay particles with a length between 1 and 2 mm were labelled with chromium, larger particles with a length between 1 and 10 mm with cerium. Cobalt-EDTA was used as a fluid marker. The animals were given the mixed labelled hay particles and labelled water as a single dose. Before and for five days after the administration, the faeces of the animals were collected as often as possible.



Fig. 1: The hippopotamus Kathi

The concentrations of chromium, cerium and cobalt in the faeces samples were determined by instrumental neutron activation analysis. After the samples had been dried and homogenized, 20–25 mg aliquots were sealed in ampoules made of highly pure silica, and, together with standard samples, were irradiated with thermal neutrons at the Berlin reactor BER II (neutron flux density $6 \cdot 10^{12} \text{ cm}^{-2} \text{ s}^{-1}$, irradiation period 2 d, decay period 3 d). Of the radionuclides thus produced, the gamma rays of ^{51}Cr , ^{141}Ce and ^{60}Co were used for the quantitative analysis.

Figs. 2 and 3 show the concentrations of the three elements in the faeces collected at different periods of time after administration of the labelled dose. From these values the mean retention time was calculated. For Kathi the mean retention time was 77.4 h for the Cr-labelled 1–10 mm long hay particles and 73.4 h for the Ce-labelled 1–2 mm long particles and for Josef 62.7 h and 60.8 h, respectively. As was to be expected, the mean fluid retention time determined by means of the Co analysis was much shorter (35 h for Kathi and 27 h for Josef).

These results are a first indication that the fore-stomach physiology of the hippos differs from that of ruminants, insofar as the former have a faster excretion of the larger particles. In this respect, hippos might be representative for other non-ruminant foregut fermenters.

The study also showed that instrumental neutron activation analysis which allows the simultaneous determination of several elements in dried biological materials without any further sample preparation, is very well suited to be applied in tracer studies using multi-elemental labelling techniques.

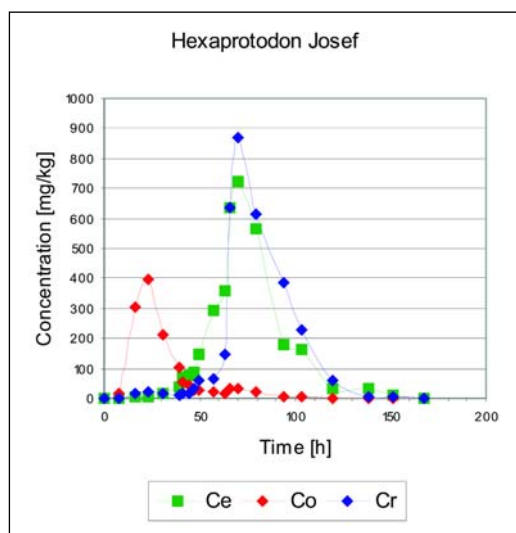


Fig. 2: Concentrations of Ce, Co and Cr in the faeces samples of Josef at different periods of time after administration of the labelled dose

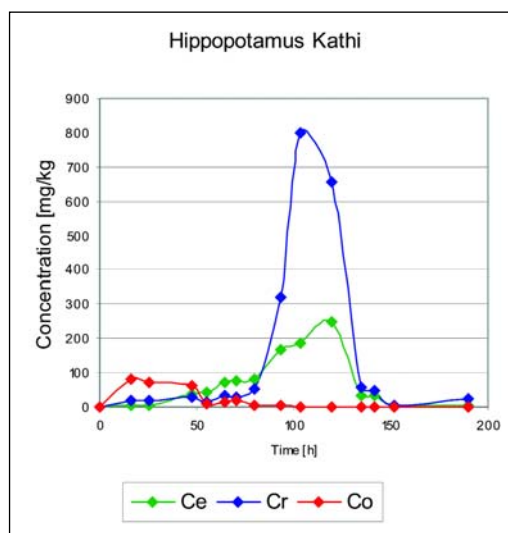


Fig. 3: Concentrations of Ce, Co and Cr in the faeces samples of Kathi at different periods of time after administration of the labelled dose

EXED – an instrument in progress

J. Peters, K. Lieutenant, D. Clemens, F. Mezei

■ HMI, SF1

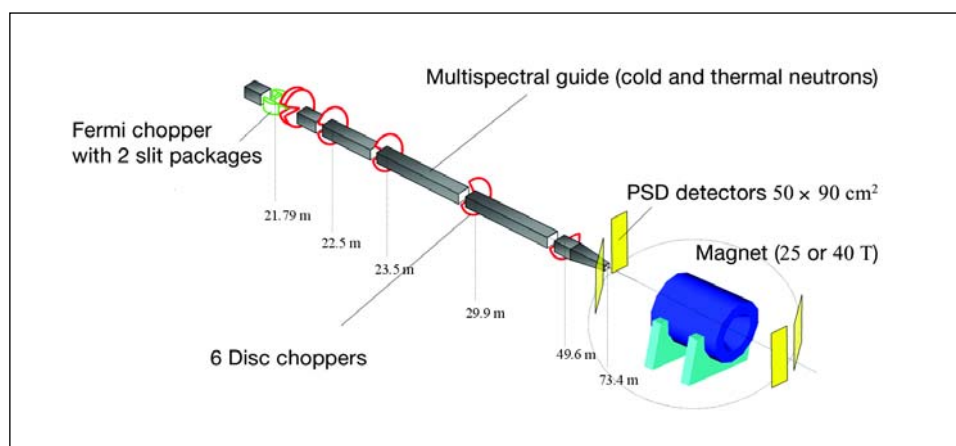


Fig. 1: Schematic view of the EXED instrument. The grey tubes correspond to a ballistic neutron guide (straight guide and the compressor). The neutron pulses are produced alternatively by a Fermi chopper (in green) or by a counter rotating double disk chopper (in red), which are exchangeable. The other disk choppers (in red) are frame overlap and a wavelength band chopper. The position sensitive gas detectors are presented in yellow and can be moved around the sample and the magnet. The blue structure is a magnet that might be used with the instruments. The sample is placed at its centre; the scattered neutrons leave in both forward and backward directions through the conical openings at the magnet's ends. The opening angles of the cones confine the range of accessible scattering angles.

The Extreme Environment Diffractometer EXED will be a central element of the instrumentation in HMI's new neutron guide hall, which is currently under construction (cf. News article on page 9). As a powder diffractometer, EXED will be mainly used for investigations of crystal and magnetic structures, in particular in substances available in form crystal powder only. In the development of this instrument several novel technologies will be applied, some of them developed at HMI. The instrument will be prepared for use with the planned 25-Tesla and 40-Tesla magnets thus contributing to HMI's position as a leading centre for the application of extreme sample environments with neutron scattering. Currently, the design of the instrument is in progress. EXED is expected to become operational by the end of 2006 and then serve as a user instrument at BENSC.

When monochromator crystals are employed in powder diffractometers, they select from the stream of neutrons incoming from the source those with a particular wavelength. The neutrons are then scattered in the sample and from the change in the direction of their motion one can deduce the momentum transmitted during the

scattering process and finally the crystal's structure. Instead of being equipped with a monochromator, EXED is based on the time-of-flight (TOF) principle. In this case, a system of choppers – rotating slotted disks – selects packages of neutrons with wavelengths in a predefined range. These neutrons are then scattered on the sample and recorded by a detector. Since the wavelength of the neutrons is correlated with their velocity and their energy does not change during the scattering process, from the time of a neutron's arrival at the detector the particle's wavelength can be inferred. From the

wavelength and the scattering angle one can calculate the momentum transfer – the scattering vector Q .

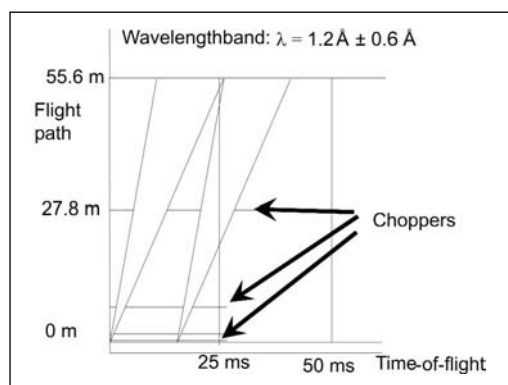


Fig. 2: Time-of-flight diagram for the chopper diffractometer. The diagonal lines correspond to neutrons with the extreme values within the chosen wavelength band of $\lambda = 1.2 \text{ \AA} \pm 0.6 \text{ \AA}$ cut by the chopper system out of the neutron stream. In this example, a wavelength band of $\Delta\lambda = 1.2 \text{ \AA}$ can be obtained, as for a larger band subsequent neutron packages would overlap.

For pulsed neutron sources the time-of-flight technique is inherent. However, compared to a common crystal monochromator instrument, it offers a number of advantages on a continuous neutron source, too:

- higher resolutions, comparable to those now achieved at synchrotron radiation sources;
- efficient measurements for crystals with small distances between the crystal planes (d -spacing);
- more efficient in terms of neutron intensity for conventionally high resolution neutron diffraction work;
- full coverage of the relevant domain of scattering vectors Q at very limited angular access in scattering angles. Thanks to the variety of wavelengths in the incoming neutron package, the whole range of relevant values of momentum transfer during the scattering process can be observed within a small range of scattering angles. This property is important as the geometry of the new magnets for extreme sample environments will strongly confine the observable range of scattering angles (see Fig. 1).

EXED will be installed on an innovative multi-spectral neutron guide – a neutron guide delivering both the thermal and the cold neutron spectrum to the sample at about 80 m from the neutron source. Computer simulations using the Monte Carlo method [1] give an estimate of the maximum flux at the sample of $3 \cdot 10^6$ n/(cm²·s), which is comparable to the flux achieved by the General Materials Diffractometer GEM at the ISIS laboratory in England. The multispectral guide allows for an incoming wavelength range of 0.7 to 20 Å, i.e. a d -spacing ranging from 0.35 – 10 Å, i.e. a momentum transfer Q domain of 0.63 – 17.9 Å⁻¹ can be studied in the high resolution back-scattering configuration at scattering angles ranging from 155 – 178°. The symmetric forward scattering range of 2 – 25° will make Q values of 0.01 – 3.9 Å⁻¹ accessible.

With a flight-path of 54 m between the chopper and the sample, the highest resolution will be achieved using a 36000 RPM curved Fermi chopper for a pulse length of 6 μs full-width half-maximum (FWHM). The resolution will be adjustable to the needs of the experiment by extending the pulse length to up to 4000 μs with the help of alternate choppers (lower resolution straight Fermi chopper and a disc chopper pair with variable slit width). The highest resolution in backscattering geometry will achieve $\delta d \sim 3.5 \cdot 10^{-4}$ Å, i.e. $\delta d/d \sim 2 \cdot 10^{-4}$ for common d -spacing in the 2 Å range. The wavelength range to be explored will be defined by the phases and angular velocities of the choppers and can be scanned continuously (for example, see Fig. 2).

The instrument has completely been simulated with the Monte Carlo software package VITESS, developed at HMI for the simulation of neutron scattering experiments [1]. First results show a good agreement with tabulated experimental data for an Al powder sample (see Fig. 3) and confirm the theoretically calculated best total resolution achievable at this instrument in backscattering direction.

[1] VITESS website:
<http://www.hmi.de/projects/ess/vitess/>

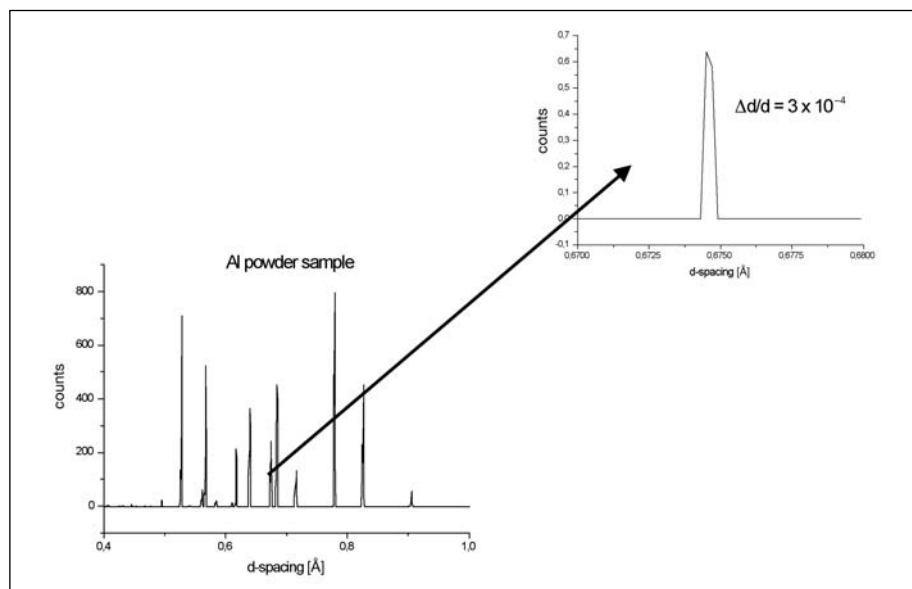


Fig. 3: Powder pattern MC simulation results (VITESS – at the lhs) for $0.7 \text{ \AA} < \lambda < 1.8 \text{ \AA}$ and $156^\circ < 2\theta < 179^\circ$ as a function of the d -spacing (the distance between parallel planes in the crystal structure). At $2\theta \approx 176^\circ$ and $\lambda = 1.34 \text{ \AA}$ (rhs), nearly the highest total resolution of $\delta d/d \sim 3 \cdot 10^{-4}$ is obtained.

Relaxation in a glassy magnet

C. Pappas¹, F. Mezei¹, G. Ehlers², P. Manuel³, A. Hillier³, R. Cywinski⁴ and I.A. Campbell⁵

■ 1 HMI, SF1 ■ 2 ILL, Grenoble, France and SNS, Oak Ridge, Tennessee, USA ■ 3 ISIS, Rutherford Appleton Laboratory, Chilton, Didcot, UK ■ 4 Physics & Astronomy Department, University of Leeds, Leeds, UK ■ 5 Laboratoire des Verres, University Montpellier II, Montpellier, France

The glass transition, characterised by a dramatic slowing down of the dynamics without any noticeable change in the spatial order, is a generic phenomenon, seen in systems as different as disordered magnets, polymers and biological substances. In spite of its universality, it is still controversial whether this is a real phase or a gradual freezing. The difficulty is due to the absence of an observable static order parameter in the low temperature phase. In fact the “snapshot” structure factor $S(Q) = S(Q, t=0)$, which reflects the short and medium range static correlations, shows no essential change when passing from the high temperature liquid or paramagnetic to the low temperature frozen glassy phase. In this situation the observation of dynamic scaling relations, which are the direct consequence of the homogeneity hypothesis in the vicinity of a critical instability can reveal the crucial signature of a true phase transition.

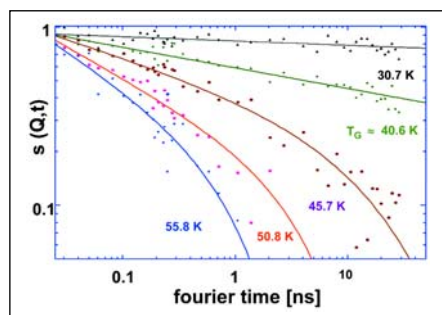


Fig. 1: Temperature dependence of the normalised intermediate scattering function $s(Q,t)$ of $\text{Au}_{0.86}\text{Fe}_{0.14}$ at $Q = 0.4 \text{ nm}^{-1}$ with the Neutron Spin Echo spectrometer IN15 (ILL) for $T = 30.7 \text{ K}$ (black), 40.6 K ($\sim T_G$, green), 45.7 K (brown), 50.8 K (red) and 55.8 K (blue) respectively. The continuous lines are the best fits to the data of a simple power law decay below T_G and of the Ogielski function $t^{-x} \exp(-t/\tau(T)^{\beta})$ above T_G .

pic times up to times, which already belong to the “long” time relaxation domain and for this reason it is the method of choice for studying glassy dynamics. NSE measures the intermedi-

ate scattering function $s(Q,t) = S(Q,t)/S(Q,t=0)$, which in spin glasses is Q -independent and delivers a direct determination of the spin autocorrelation function $q(t)$.

Figure 1 shows in a log-log scale the NSE spectra of the classical metallic Heisenberg spin glass $\text{Au}_{0.86}\text{Fe}_{0.14}$ at $Q = 0.4 \text{ nm}^{-1}$ as measured at the IN15 spectrometer of the ILL with a wavelength of 0.8 nm . The spectra extend over a dynamic range of three orders of magnitude and by combining these data with spectra obtained at a wavelength of 0.45 nm at the BENSPECT spectrometer SPAN the time domain of the observation is extended up to almost 4 decades (Fig.2). $s(Q,t)$ is strongly non-exponential and the large dynamic range allows one for the first time to distinguish between the different forms, which have been suggested to describe the relaxation [1].

From quite general scaling arguments relaxation above a continuous phase transition must be of the form $t^{-x} f(t\tau(T))$, where $\tau(T)$ diverges as $(T-T_G)^{-z}$, so that at the transition it reduces to a simple power law with an exponent x related to the standard critical exponents through $x=(d-2+\eta)/2z$, with η the Fisher exponent, d the space dimensionality and z the dynamical exponent. As seen in Figs. 1 and 2, $s(Q,t)$ follows a simple power law decay at T_G (~ 40.6), $s(Q,t) \propto t^{-x}$, with $x = 0.116 \pm 0.007$, which is in excellent agreement with $x = 0.116 \pm 0.026$ the value calculated from the well established exponents of Heisenberg spin glasses, known from macroscopic susceptibility measurements [2]. This is the first time that it was possible to verify critical scaling in a glassy system by relating quantities of very different nature and measured by different methods on very different time scales, namely the microscopic time dependence of the autocorrelation function at times between the microscopic time and 10^{-7} s on the one side and the macroscopic a.c. susceptibility at time scales greater than 10^{-3} s together with the static non-linear susceptibility on the other.

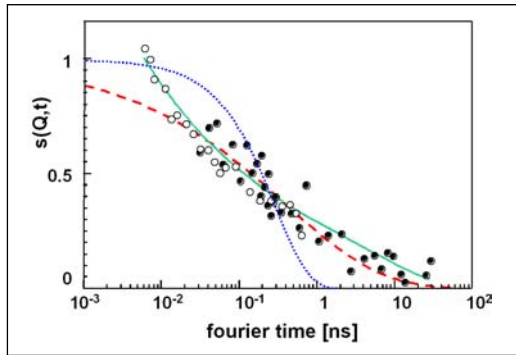


Fig. 2: NSE spectra of $\text{Au}_{0.86}\text{Fe}_{0.14}$ collected at the ILL spectrometer IN15 (full symbols) and at the BENSIC spectrometer SPAN (open symbols) at 45.6 K. The continuous green line represents the fit of an Ogielski function $t^x \exp(-t/\tau(T)^\beta)$. The red dashed and blue dotted curves correspond to a stretched exponential and a simple exponential decay respectively.

Above T_G neither a pure exponential nor a stretched exponential decay describe the relaxation. In fact, the spectra are impressively similar to the $q(t)$ found in large scale Ising spin glass simulations by A. Ogielski [3], which revealed the existence of a phase transition in three-dimensional Ising spin glasses. There is a clear power law decay at short times with a cut-off at longer times, which is not exponential. Ogielski chose to represent $f(y)$ by the stretched exponential or KWW function, familiar in fragile glass dynamics, and obtained excellent fits with $q(t) \propto t^{-x} \exp(-t/\tau(T)^\beta)$ and β tending to $1/3$ at T_G , as expected from general arguments in glassy systems [4]. The power law part of this so-called Ogielski function describes the main part of the relaxation above T_G and the NSE spectra lead to an accurate determination of the exponent x . On the other hand, the stretched exponential only describes the tail of the relaxation and the parameters $\tau(T)$ and b are obtained to low accuracy.

A full description of the relaxation was made possible by complementing the NSE results with zero field Muon Spin Relaxation (μSR) measurements done on the very same sample. All μSR spectra strongly deviated from a simple exponential form and the non-exponential relaxation stretches over an unusually broad temperature domain up to almost room temperature, i.e. $\sim 6 T_G$. The fit to the stretched exponential form leads to the temperature dependence of the exponent β , seen in Fig. 3. Close to T_G β tends to $1/3$ but becomes even smaller than $1/3$ in the very vicinity of T_G , which clearly indicates the more complex relaxation than a simple stretched exponential form found with NSE.

The μSR spectra inform on the long time tail of the Ogielski function, which describes the spin autocorrelation function above T_G . When fitting the “log time” part of the NSE spectra to a simple stretched exponential the values of β are in excellent agreement with those found by μSR (Fig. 3). Muon depolarisation is due to the interaction with the Fe local magnetic moments. NSE on the other side measures the spin autocorrelation function and the collective dynamics of Fe spins. The agreement between μSR and NSE shown in Fig. 3 should therefore not be taken for granted. It is the direct consequence and at the same time an additional proof of the intrinsically homogenous nature of the non-exponential relaxation in spin glasses.

For intensity reasons, NSE measurements were only possible close to T_G and below. The μSR spectra on the other side were recorded up to room temperature. They reveal the existence of two distinct regimes with a clear crossover around 60 K, which can be seen as the crossover between the low temperature critical spin glass relaxation and the high temperature Arrhenius-like relaxation. β increases very slowly above ~ 60 K and only around room temperature the relaxation becomes exponential with $\beta \sim 1$. This anomalous paramagnetic relaxation can arguably be identified with the Griffiths phase, which should extend up to the Curie temperature of the non-diluted reference ferromagnetic phase. The very high Curie temperature of pure Fe, 1140 K, would therefore explain the extremely large temperature domain of non-exponential relaxation in this disordered system.

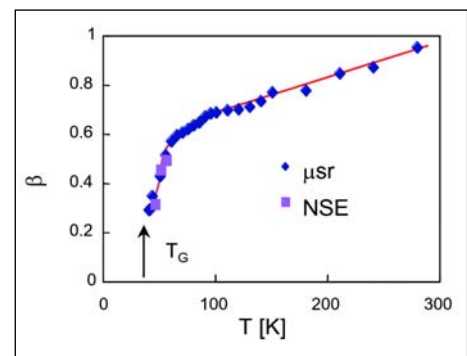


Fig. 3: Temperature dependence of the exponent β deduced by fitting the stretched exponential function $\exp(-t/\tau(T)^\beta)$ to the muon depolarisation spectra. The squares were obtained by fitting the tails of the Neutron Spin Echo spectra to the stretched exponential function.

- [1] C. Pappas, F. Mezei, G. Ehlers, P. Manuel, I.A. Campbell, Phys. Rev. B **8**, 054431 (2003)
- [2] L. P. Lévy, Phys. Rev. B **38** (1988) 4963
- [3] A.T. Ogielski, Phys. Rev. B **32** (1985) 7384
- [4] L.W. Bernardi, S. Prakash and I.A. Campbell, Phys. Rev. Lett. **77** (1996) 2798

Pre-equilibrium emission in 1.2 GeV proton-induced spallation reactions

C.-M. Herbach, D. Hilscher, U. Jahnke

■ (HMI, SF1) for the NESSI-collaboration: HMI, FZJ, GANIL, Univ. of Warsaw, Univ. of Rochester

Spallation reactions¹ induced by medium-energy proton beams have a wide field of interest in science as well as in practical application: in cosmology and astrophysics, cosmic ray physics, planetary and geochemical science, and – last but not least – in nuclear physics on the one hand, and for generation of neutrons in spallation neutron sources on the other hand. Spallation neutron sources, such as the future European Spallation Source ESS, in turn, are needed as a favorable alternative to conventional nuclear reactors in basic research, for the transmutation of nuclear waste or possibly to replace conventional nuclear power stations by accelerator-driven hybrid systems.



Fig. 1: The NESSI detector at the COSY accelerator.

During recent years the NESSI collaboration (HMI, FZJ, GANIL, Univ. Warsaw and Univ. Rochester) investigated systematically GeV-proton induced spallation reactions [1–7]. The motivation for this program is twofold. First, the above mentioned applications call for an experimental validation of the underlying basic spallation reaction models in order to ensure that the present models and codes have reached an adequate precision which would allow one to perform reliable simulation calculations. For instance, structural materials of the target station of a spallation neutron source, which are exposed to GeV proton beams, must withstand the intensive generation and retention of large levels of hydrogen and helium, the amount of which has to be calculated reliably in such a complex environment. Second, the interest of nuclear physics stems from the fact that proton as well as antiproton induced reactions generate nuclei with high thermal excitation energy with a minimum of compression, deformation, and spin – quite in contrast to heavy

ion induced reactions which excite the latter collective degrees of freedom rather strongly. These properties enable one to study the decay of highly and *thermally* excited nuclei, in particular fission at high excitation energies.

Spallation reactions can be considered as three-step reaction mechanisms. The first step is treated by an intra nuclear cascade (INC) [8] which excites the nucleus to high excitation energies depending on the impact parameter. During a second intermediate step, particles are emitted prior to the attainment of a statistical equilibrium and in the third step the equilibrated nucleus de-excites by light-particle evaporation. While the first and the last step are well understood and described in various models the second step, the intermediate pre-equilibrium emission of composite particles, is presently not well understood and theoretically discussed in terms of very different assumptions. Furthermore, the pre-equilibrium emission of fast composite particles in spallation reactions has so far not been studied systematically and very few experimental results are available. The neglect of this reaction phase in simulation calculations, however, turned out to be a too crude simplification. In the reaction $p(2.5 \text{ GeV}) + \text{Au}$, for example, more than 50 % of the deuterons are emitted from pre-equilibrium [5] and the total energy carried off by fast composite particles amounts to about 95 MeV.

Here we give a brief overview about preliminary results which have recently been obtained with the NESSI detector (Fig. 1) at the COSY accelerator in FZ Jülich for the reaction of 1.2 GeV protons with target nuclei of Al, Ti, Fe, Ni, Cu, Zr, Ag, Ho, Ta, W, Au, Pb, and Th. The data have been measured with six triple- ΔE -E telescopes [6] consisting of three silicon detectors (25 μm , 80 μm and 1000 μm) backed by a 7 cm long CsI crystal which were positioned at angles of 30°, 75°, 105°, and 150°.

¹ In 1947 Glenn T. Seaborg coined the term spallation for reactions in which a heavy nucleus is hit by a highly energetic light projectile, e.g. a proton, which leads to the ejection of a large number of light particles (neutrons, protons, alpha particles) or heavier fragments.

Energy spectra of $^{1,2,3}\text{H}$ and ^3He observed in the reaction $p(1.2\text{GeV})+\text{Zr}$ are compared in Fig. 2 with results of simulations with the code INCL2.0 [8] for the Intra-Nuclear Cascade and the code GEMINI [9] for the subsequent statistical evaporation. The calculated yields of evaporated particles have been scaled to fit to the experimental data. They are used to separate the contributions from pre-equilibrium emission in the measured spectra and to correct the data for losses due to the lower energy detection threshold. The angular dependence of the spectra reveals that the pre-equilibrium emission occurs predominantly into the forward hemisphere while the evaporation is almost isotropic.

The experimental results for the integrated cross sections of evaporated particles are summarized in the upper panel of Fig. 3. The data are well reproduced by the predictions of the simulation calculation with INCL2.0+GEMINI.

The relative contribution of the pre-equilibrium emission σ_{pre} to the total production $\sigma_{\text{eva}}+\sigma_{\text{pre}}$ of composite particles is shown in the lower panel of Fig. 3. The data indicate that the contributions of pre-equilibrium emission are slightly enhanced for heavier targets. The smallest

portion of $\sigma_{\text{pre}}/(\sigma_{\text{eva}}+\sigma_{\text{pre}})$ is found for ^4He with 10–15 %, while the other contributions are as high as 40–60 % for ^2H and ^3He and 25–40 % for ^3H . These observations together with our previous results [5] for $p(2.5\text{ GeV})+\text{Au}$ definitely call for a consideration of fast composite-particle emission in present reaction models. A refined evaluation of the data will be devoted to the evolution of pre-equilibrium emission with excitation energy.

- [1] L. Pienkowski et al., Phys. Rev. C **56**, 1909 (1997).
- [2] D. Hilscher et al., Nucl. Instr. Meth. A **414**, 100 (1998).
- [3] M. Enke et al., Nucl. Phys. A **657**, 317 (1999).
- [4] A. Letourneau et al., Nucl. Instr. Meth. B **170**, 299 (2000).
- [5] A. Letourneau et al., Nucl. Phys. A **712**, 113 (2002).
- [6] C.-M. Herbach et al., Nucl. Instr. Meth A **508**, 315 (2003).
- [7] D. Hilscher et al., J. Nucl. Mater. **296**, 83 (2001).
- [8] J. Cugnon et al., Nucl. Phys. A **620**, 475 (1997).
- [9] R.J. Charity et al., Nucl. Phys. A **483**, 391 (1988).

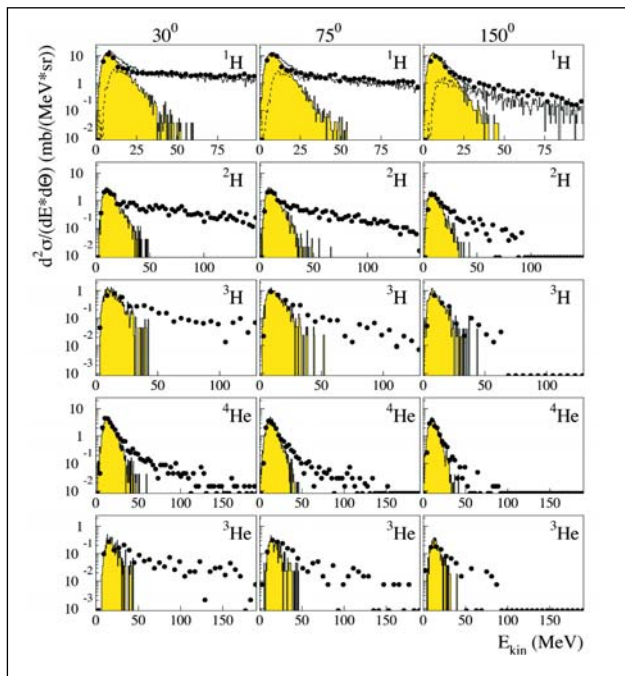


Fig. 2: Kinetic energy spectra of $^{1,2,3}\text{H}$ and ^3He as measured for $p(1.2\text{ GeV})+\text{Zr}$ at 30° , 75° , and 150° (dots). Results from simulations (INCL2.0+GEMINI) are plotted as gray area for evaporated particles and as open area (dashed line) for INC protons.

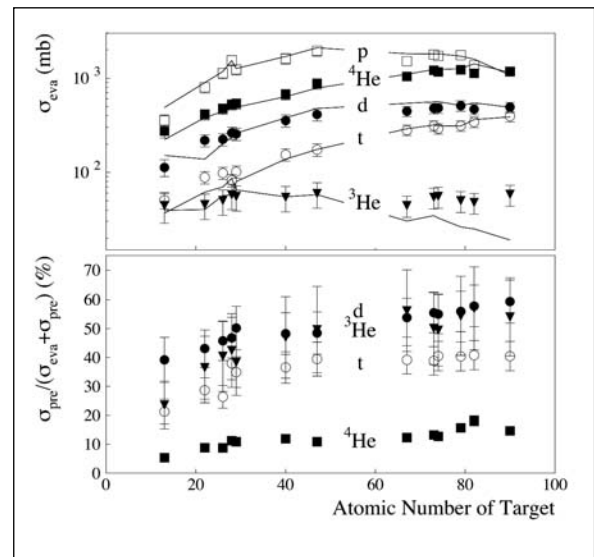


Fig. 3: Integrated production cross sections of $^{1,2,3}\text{H}$ and ^3He in reactions with 1.2 GeV protons, plotted as a function of the atomic number of the target nucleus. The upper panel shows the measured cross sections (symbols) for evaporated particles in comparison with results from INCL2.0+GEMINI simulations (lines); the cross sections for pre-equilibrium emission of composite particles (lower panel) are given relative to the total yield.

Surface and interface magnetization of ultrathin films

H. Maletta
 ■ HMI, SF2

Today's magnetic materials are not the bulk materials of old, but atomically engineered structures of nanometer dimensions with ferromagnetic, antiferromagnetic and non-magnetic components. This development is clearly fueled by the already successful applications in modern information technology and the further need for even smaller magnetic devices. At the same time, confinements on the nanoscale can give rise to new and fascinating phenomena in magnetism which are challenging to be understood from fundamental physical aspects, too. The study of such advanced materials requires new experimental techniques that are capable of probing them on the nanometer length scale. Our group at HMI has studied various properties of such materials by applying both the neutron beams at BENSC and the synchrotron x-rays at the new HMI-undulator beamline at BESSY.

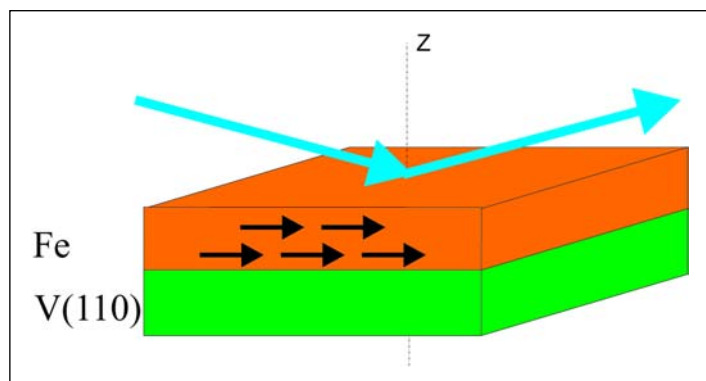


Fig. 1: Schematic view of the reflection measuring geometry with an ultrathin iron (Fe) film grown on a vanadium (V) crystal. Blue arrows: incoming and reflected beams. Black arrows: Orientation of the magnetic moments in the Fe layer.

Reflectometry with polarized neutrons

Reflectometry with polarized neutrons (PNR) is a well established technique for the study of thin film magnetism. One measures the reflectivity – the ratio of reflected neutron intensity to the total incoming intensity – as function of the incident angle at very small angles (grazing incidence). Due to the geometry (Fig. 1), one is primarily sensitive to the density or magnetization depth profile perpendicular to the film surface (in z direction). We have successfully developed a unique option [1] where one can measure the properties of even uncapped thin films by *in-situ* PNR, i.e. the preparation, structural characterization and PNR measurement are performed in the same UHV chamber. As a first example we determined the absolute value of the magnetization of thin epitaxial iron (Fe) films with a free surface grown on a vanadium V(110) single crystal as function of the thickness of Fe. In addition, we found that the magnetization is changed in value when the sample is capped with a V layer.

X-ray resonant magnetic reflectometry

In a second step, we studied the same samples with synchrotron x-rays [2] on the new HMI undulator beamline at BESSY. It provides highly intense x-rays which are variable in polarization (linear and circular) and tunable in energy from 200 eV to 1800 eV. Whereas PNR is well suited to measure the absolute value of the total magnetization, the study with polarized soft x-rays enables one to separate the element-specific components via the magnetic circular dichroism effect (XMCD). Indeed, we detected a small induced V magnetization being antiparallel to Fe. Our XMCD absorption measurements are consistent with details of the Fe magnetization indicated in Fig. 2. In order to confirm the magnetic details at the free surface and interface we are just preparing the next experiments where we will perform the X-ray resonant magnetic reflectometry (XRMR) method.

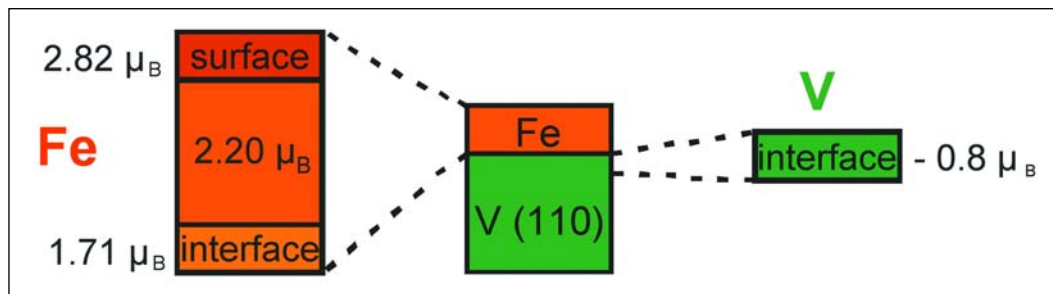


Fig. 2: Details of the magnetization of Fe/V(110) (schematic view).

The XRMR method is a new tool which has been developed by us in collaboration with the MPI Stuttgart [3] on the basis of our knowledge on PNR. It utilizes the effect that the magnetic cross section of x-rays is resonantly enhanced by orders of magnitude near an absorption edge. Recently, the first experiments were successfully performed on a sandwich sample Pt/Co/Cu, i.e. on a 2 nm thin cobalt (Co) film grown on a copper (Cu) substrate and capped with a platinum (Pt) layer. The quantitative results summarized in Fig. 3 indicate that the magnetic moment of Co is enhanced by up to 30 % near the interface to the Pt layer, but reduced by 25 % near the Cu substrate. The element specific technique enabled us also to tune the x-ray energy to the value of the Pt absorption edge revealing a small induced magnetization in the Pt cap layer which decays exponentially within a 1 nm depth. Hence, it is demonstrated that high sensitivity for small magnetic moments can be achieved by applying XRMR.

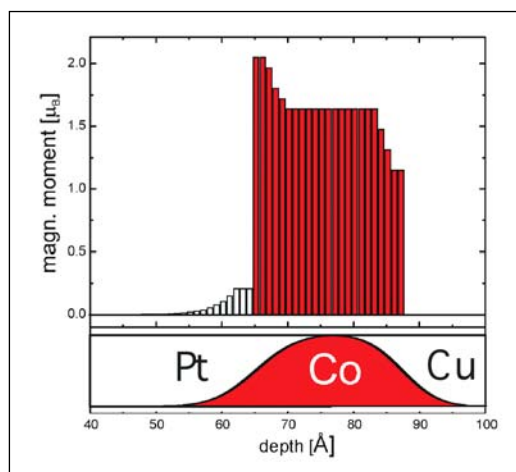


Fig. 3: Magnetization depth profile of Pt/Co/Cu (schematic view) obtained by XRMR at the Co and Pt site. The analysis includes the interface roughness as indicated below.

Outlook

These methods are considered as new tools for systematic investigations of details of magnetization properties at buried interfaces and free surfaces as a function of roughness or ligand layer composition of various magnetic layered systems. Work is underway in a collaboration in order to interpret the results quantitatively by calculations of the effects of reduced coordination numbers and hybridizations on the magnetic moment value. Nowadays, such systems work as basic components of devices in information technology for instance for magnetic sensors and magnetic random access memories (MRAMs) due to the giant magnetoresistance (GMR) effect, and may be relevant in future *spin-tronic* devices.

- [1] T. Nawrath, H. Fritzsche, F. Klose, H. Maletta, Phys. Rev. B **60**, 9525 (1999).
- [2] D. Schmitz, J. Hauschild, P. Imperia, Y.T. Liu, H. Maletta, J. Magn. Magn. Mater. **269**, 89 (2004); and to be published.
- [3] J. Geissler, E. Goering, M. Justen, F. Weigand, G. Schütz, J. Langer, D. Schmitz, H. Maletta, Phys. Rev. B **65**, 020405 (R) (2002); and submitted for publication.

Field distorted magnetic spirals: a neutron diffraction study of the magnetism in the frustrated quantum antiferromagnet CsCuCl_3

N. Stüßer¹, U. Schotte¹, A. Hoser²

■ 1 HMI, SF2 ■ 2 Institut für Kristallographie, RWTH Aachen

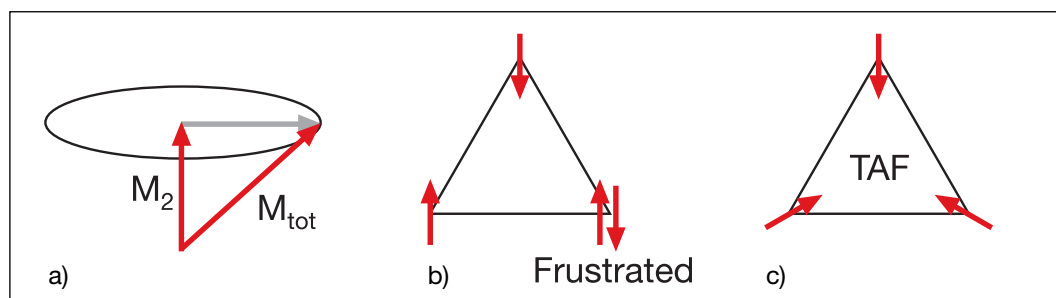


Fig. 1: a) In quantum mechanics only one component of the magnetic moment M_{tot} is defined e.g. M_z . The perpendicular components are uncertain and can be considered to fluctuate on the ellipse. These fluctuations are basically a result of Heisenberg's uncertainty relation. b) Geometrical frustration: Three spins located at the corners of a regular triangle cannot simultaneously order antiparallel to each other. c) If moments are free to rotate in a plane antiferromagnetic coupling between neighbours leads to the formation of a triangular antiferromagnet (TAF). All spins are inclined by 120° to their neighbours.

Since the foundation of quantum mechanics the study of quantum effects has been a subject of continuous interest in fundamental solid state physics. In particular magnetic systems have served as models to test theories in this field. For magnetic systems quantum fluctuations can play an important role in the formation of magnetic structures. Differing from the classical description, in quantum physics a magnetic moment can never be completely aligned. Only a part of the total moment can be aligned along one direction and the perpendicular components are uncertain. One can consider this situation as a moment fluctuating around some mean value determining the size of the ordered moment (Fig. 1a). Quantum theory tells us that these fluctuations are relatively enhanced for small moments which are found e.g. at Cu^{2+} -ions. Another topic of current interest is the investigation of systems with geometrical frustration [1]. In geometrically frustrated systems, two body interactions like couplings of magnetic spins can not all be realized due to some special geometry of the underlying lattice of the spins (Fig. 1b,c). This is realized in CsCuCl_3 which will be presented now showing our most recent results on the study of quantum effects on a system with geometrical frustration.

Since a few years, we have been investigating the magnetic structure of CsCuCl_3 crystals as a function of temperature and magnetic field [2]. Different magnetic phases could be identified and could be related to the influence of quantum

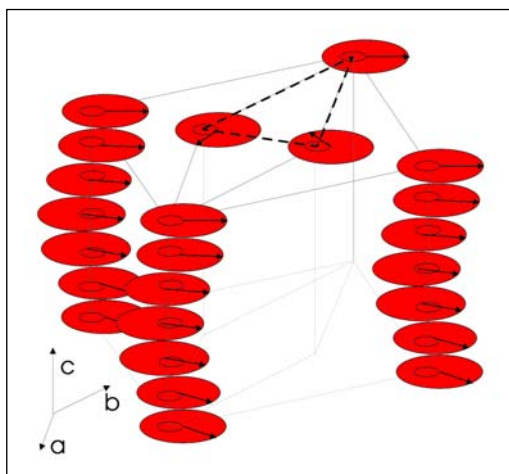


Fig. 2: Magnetic structure of CsCuCl_3 below 10.6 K. A long wavelength spiral is formed in c direction. A triangular 120° structure is present in the ab plane.

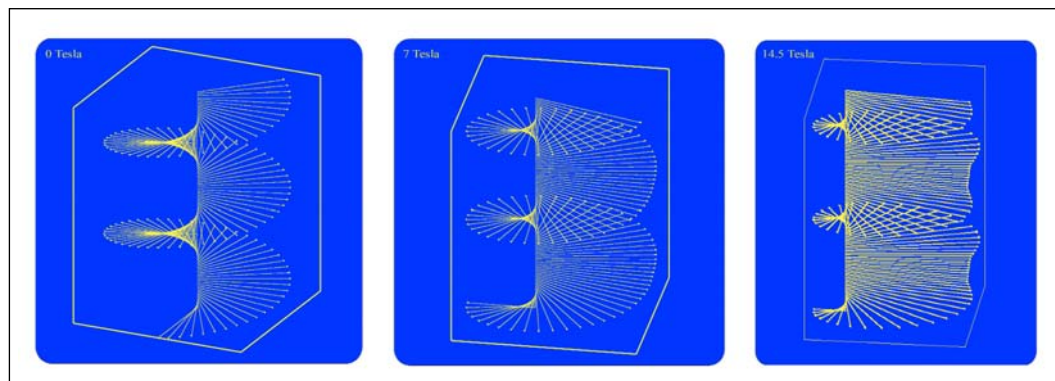


Fig. 3: Magnetic spiral of CsCuCl_3 at 0 T, 7 T, and 14.5 T

fluctuations. Let us first briefly introduce the magnetic structure of CsCuCl_3 at zero field (Fig. 2). Below 10.6 K the spins at the Cu^{2+} -ions are magnetically ordered: a triangular spin arrangement with 120° -type structure is formed in the ab plane and an incommensurate spiral occurs along the c axis with a repetition length of about 71 layers. Fig. 2 shows only a small section of the structure which should be repeated in the ab plane and extended along c . The spiral is a result of a competition between a dominating ferromagnetic coupling of adjacent spins along c which tries to keep spins parallel, and a so called antisymmetric coupling which tries to keep spins perpendicular. The compromise is an incommensurate winding of the spins with a pitch angle of about 5° between neighbours. The 120° structure in the ab plane is caused by geometrical frustration. The antiferromagnetic coupling which favours an antiparallel spin alignment of neighbours cannot be satisfied simultaneously for three spins on a triangle. This situation is called frustration. If the spins are free to rotate in the ab plane – as is the case for CsCuCl_3 – the 120° structure will correspond to the minimum in energy. It is found experimentally that the ordered spins have a reduced moment in agreement with theoretical calculations [3, 4]. The spin reduction is a direct consequence of quantum fluctuations together with the geometrical frustration. We were interested to see how the application of a magnetic field changes the magnetic structure for such a frustrated system in order to test recent theoretical predictions. Therefore, diffraction experiments were performed at a neutron spectrometer located at our BER II reactor of the Hahn-Meitner Institute. A beam of neutrons with a well defined energy was diffracted at a single crystal of CsCuCl_3 . The crystal was mounted in one of our high field magnets which allows the application of field strengths up to 14.5 T. In order to study the quantum effects which become significant close to zero temperature, the experiments were car-

ried out at 2 K and the diffracted neutrons were measured as a function of scattering angle. We analysed the diffraction patterns and yielded a detailed picture of the magnetic structure which cannot be obtained by any other experimental technique.

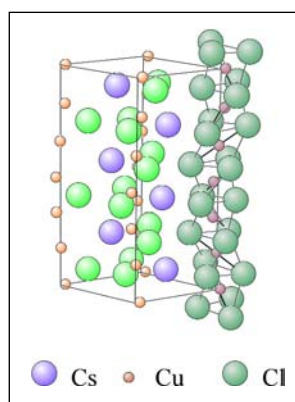


Fig. 4: CsCuCl_3 crystal structure

The pictures of the spirals distorted by an applied field for different field strengths are shown in Fig. 3. Our analysis clearly revealed that the field distorted-spirals can be described as a rotation of spins towards the field direction and the spin reduction is lifted for those spins pointing towards the field direction. Spins in opposite direction spread apart and the spin reduction has even increased for spins pointing opposite to the applied field. This behaviour can be found in principle in the whole phase diagram since thermal fluctuations have a similar effect as quantum fluctuations.

- [1] A. P. Ramirez, *Handbook of Magnetic Materials*, 13 (2001).
- [2] N. Stüßer, U. Schotte, A. Hoser, M. Meschke, M. Meißner, J. Wosnitza, *J. Phys. Condensed Matter* **14**, 5161 (2002) and references therein.
- [3] K. Adachi, N. Achiwa, M. Mekata, *J. Phys. Soc. Japan* **49**, 545 (1980).
- [4] N. Elstner, R. R. P. Singh, A. P. Young, *Phys. Rev. Lett.* **71**, 1629 (1993).

Neutron tomography at HMI

N. Kardjilov¹, A. Hilger¹, I. Manke¹, M. Strobl², W. Treimer²

■ 1 HMI, SF3 ■ 2 Technische Fachhochschule Berlin (TFH)

Introduction

Neutron tomography is a powerful non-destructive method for the investigation of a large variety of different objects. It allows one to visualize the inner volume of a sample without destroying or dismantling it. The tomography principle is based on the mathematical reconstruction of the 3-dimensional volume from 2-dimensional projections collected while the sample is rotated around a defined axis.



Fig. 1a: 3D-tomography image of a Lithium Iodide battery. Lithium distribution (left) and general view (right)

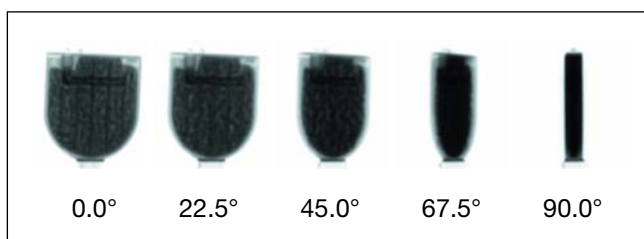


Fig. 1b: Some of the 200 single neutron-radiography projections used for the 3D-tomography reconstruction shown in Fig. 1a.

For the collection of the projection set, various kinds of transmission radiation can be used (for instance X-rays, positrons, neutrons etc). The various rays used in these experiments differ in their interaction mechanism with matter. As electrically neutral particles, neutrons interact directly with the atomic core. This is not the case for X-rays, which interact mainly with the electronic shell of the atom. The different interaction mechanisms of neutrons and X-rays with matter make neutron tomography a complementary technique to the classical X-ray tomography.

In contrast to tomography with X-rays, tomography imaging with cold neutrons is – on the one hand – highly sensitive to light elements and organic materials. On the other hand, cold neutrons pass easily through metals and other materials composed of heavy elements.

Neutron radiography setups are usually placed at multipurpose, high-flux neutron sources as nuclear research reactors or spallation sources. Therefore, the design and construction of a new neutron radiography facility is a large-scale, long-term project including the optimization of a great number of parameters concerning the beam geometry, the shielding design, the electronic control systems and many others.

A new tomography facility with cold neutrons is under construction at the reactor BER II of the Hahn-Meitner Institute, Berlin. The new beam line is placed at the end of a curved neutron guide which faces the cold neutron source of the reactor. The presence of a neutron guide helps achieve an extremely high cold neutron flux in the order of approx. 10^9 n/cm²s at the sample position (30×50 cm²) with a negligible background of gamma radiation and fast neutrons. These conditions are very suitable for investigations of strongly absorbing samples or real-time imaging of fast processes. The first test experiments at this measuring position have been already performed. Some of them are presented below.

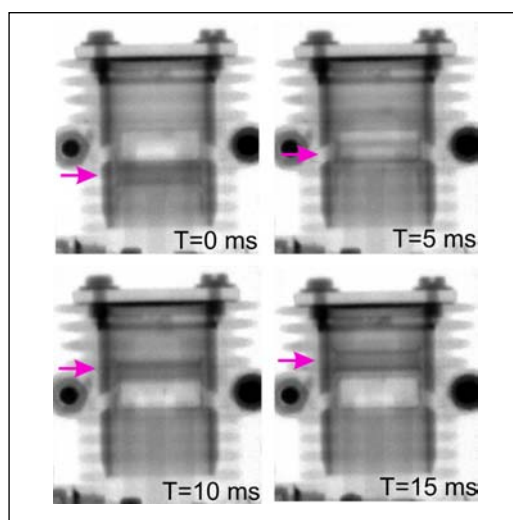


Fig. 2: Four neutron-radiography snapshots of a combustion engine at different piston positions. The arrows show the position of the piston. The experiment was performed at a rotation speed of 1110 rpm. The exposure time was 1 ms. For a defined piston position 200 images were recorded. The time delay between two piston positions was set to 1 ms.

Tomography investigation of a Lithium Iodide battery

Lithium (Li) has one of the highest attenuation coefficients for cold neutrons among the elements. So the task to investigate a Lithium Iodide (LiI) battery by means of neutron tomography was a challenge for the recently established tomography facility at HMI. Despite the difficulty that for some of the 2-dimensional projections the neutrons had to pass through almost 3 cm of LiI, it was possible to successfully reconstruct the 3-dimensional image (Fig. 1). The results of this investigation may help increase the life-time of LiI batteries used in pace-makers.

Real-time imaging

As a test sample for the real-time imaging experiment, a model aircraft combustion engine was investigated. The dimensions of the motor were ($W \times H \times T$) $70 \times 70 \times 30 \text{ mm}^3$. For the first tests, the engine was driven by a coupled electromotor.

Data collection was based on the so-called stroboscopic method for investigations of repetition processes: a set of images was recorded exactly at the same position of the piston in the cylinder. After adding up all the images for the corresponding piston position, an average snap shot with better statistics was obtained.

The whole combustion cycle was visualized by such “frozen” snap shots. Images at four piston positions are shown in Fig. 2. The next step in this work will be to investigate the fuel injection in a running motor driven by a combustion process.

Geological samples

In a further experiment, the density variation and the distribution of different minerals in a granite sample was investigated. This information gained helps make conclusions about the formation of granite. In this case, the presence of the mineral kaolinit (marked with orange in Fig. 3) in the sample is an evidence that the material underwent a hydrothermal alteration. This was probably due to a flow of hot water through it, which caused the transformation of the large feldspar crystals frequently presented in granite into kaolinit: $\text{KAlSi}_3\text{O}_8 + \text{H}_2\text{O} \rightarrow \text{Al}_2\text{Si}_2\text{O}_5(\text{OH})_4$. This kind of experiments may help find a precise quantitative classification of different types of geological materials.

Future developments

In the near future a new experimental station for neutron tomography will be built at HMI. Here, a better collimation of the neutron beam will be achieved with the help of a system of apertures. In this way, the spatial resolution of the tomography experiment will be improved from the current value of $250 \mu\text{m}$ to $100 \mu\text{m}$. Further improvements of the resolution will follow from the application of advanced neutron imaging techniques such as energy-selective and phase-contrast neutron imaging as well as imaging with polarized neutrons.

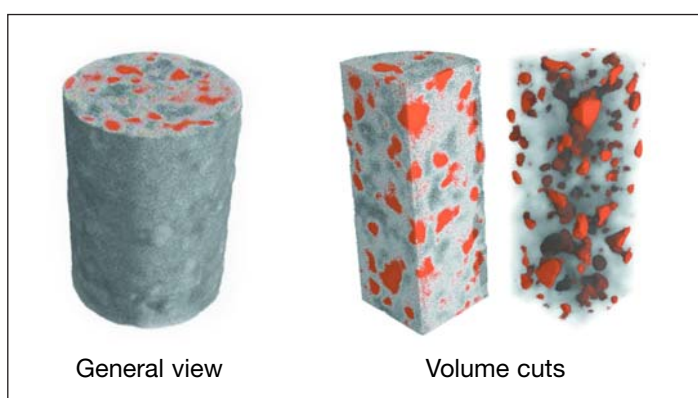


Fig. 3: The tomographic reconstruction of a granite cylinder shows the spatial distribution of the mineral kaolinit ($\text{Al}_2\text{Si}_2\text{O}_5(\text{OH})_4$) in the sample (orange). The presence of four hydroxyl groups in the chemical composition leads to a strong contrast for Kaolinit crystals in the tomography reconstruction as neutrons are strongly scattered by hydrogen.

Characterisation of Precipitates in a Stainless Maraging Steel by Three-Dimensional Atom Probe and Transmission Electron Microscopy

N. Wanderka, S. Höring

■ HMI, SF3

The three-dimensional atom probe (3 DAP) is the best technique to investigate the early stages of precipitation with nano-sized deviations from the homogeneous composition. In the present case this technique was used for the study the influence of small differences in the composition on the precipitation behaviour of a maraging steels.

Maraging steels is the generic term used for low-carbon steels forming precipitates in the martensitic phase during tempering. The term is a combination of *martensite* and *ageing*. Owing to an excellent combination of high strength and hardness, ductility and toughness, combined with good corrosion resistance, stainless maraging steels are used in many technological sectors where weight saving is of great importance such as aerospace and automotive.

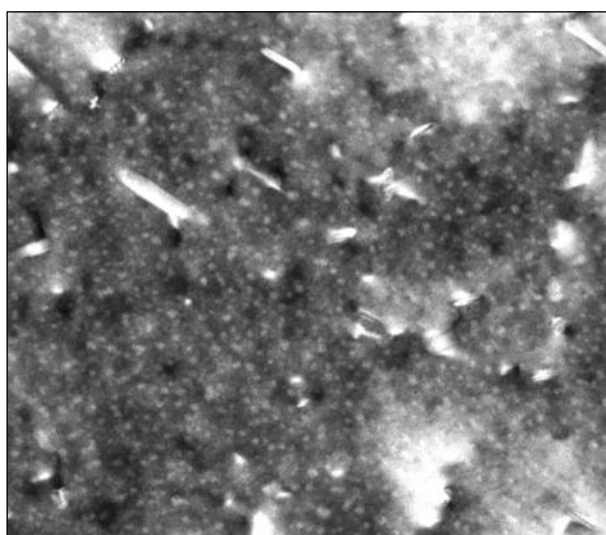


Fig. 1: TEM bright field image of the model alloy of maraging steel aged at temperature of 475°C for 100 h.

Technical steels are mixtures of very large numbers of alloying elements, some of them in very small quantities. In addition to that, maraging steels are characterized by low carbon content. Small variations in the composition of the alloying elements can change their precipitation behaviour drastically. Depending upon composition and heat treatment, a variety of different precipitates will be formed. In the present case, a model alloy for maraging steel with the composition 75.1Fe-13.1Cr-8.4Ni-1.1Si-0.96Ti-0.7Al-0.5Mo-0.1Mn-0.05C (at. %) was investigated. The 3 DAP analysis was combined with transmission electron microscopy (TEM) which is able to identify the crystallographic structure of precipitates and to give information about the number densities and volume fractions of different kinds of precipitates on a larger scale.

The investigations were concentrated on the chemical analysis of the phases after different heat treatments at 475°C. The alloy was aged at 475°C for 12 h and for 100 h. The longer time was necessary for the production of sufficiently large particles for the TEM investigations. The composition of the small precipitates (not shown here) is 44.7Fe-5.1Cr-26.1Ni-5.7Si-10.5Ti-1.7Al-0.6Mo (at. %). I.e. they are rich of Ni, Al, Ti and Si. The number density of the small precipitates is about $8.3 \cdot 10^{24} \text{ m}^{-3}$ as estimated from the number within the volume analysed by 3DAP.

The typical microstructure of the alloy after 100 h aging time is shown in the TEM micrograph in Fig. 1. Besides small spherical precipitates embedded in the matrix, larger needle- or plate-like particles are visible. In Fig. 2 the three dimensional reconstruction of the positions of Ni, Al and Ti atoms is presented for the same state of the material. Several atom clusters can be identified. Some of them contain more than 20 at. % Cr. The composition of the Cr rich particles is 46,5Fe-40,9Cr-7,3Ni-0,9Si-0,8Ti-0,4Al-0,6Mo-2,6Mn-0,5C (at. %). In addition to these particles, regions enriched in Ni, Al and Ti are also visible. The composition of the small spherical Ni-rich particles is almost as in the material aged for 12 h. These particles do not grow much, i.e. from 2.5–3 nm to 4 nm during extended heat treatment (12 h to 100 h). The larger Ni rich particles (> 15 nm) in the middle and the upper left corner of the analysed volume have the composition: 23,4Fe-6,0Cr-49,3Ni-1,5Si-6,0Ti-10,6Al-2,7Mo-Mn (at.%).

In Fig. 3, the concentration depth profiles of Cr, Ni, Fe, Al and Ti in two precipitates and the matrix are presented. They were taken along the indicated small box (shown also in Fig. 2). This box was aligned approximately perpendicular to the interface between Ni- and Cr rich precipitates. The concentration values were calculated for slices 0.4 nm thick. In our case, the first formed crystalline precipitate is rich in Si, whereas in a further steel of similar composition the formation of Ni₃Ti precipitates has been found [1, 2].

The comparison of the present results with literature on the maraging steels IRK91 [3, 4] and on a steel free of Co [1, 2] shows that the precipitation behaviour of these 3 maraging steels differs significantly, though their composition shows only small variations.

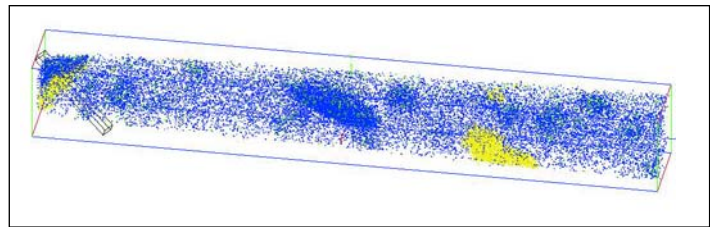


Fig. 2: Three dimensional reconstruction of Ni (blue), Ti (green), Al (dark green) atom positions in the analysed volume $11 \times 11 \times 92 \text{ nm}^3$. Cr rich areas (yellow) with 20 at.% Cr concentration are displayed in the same volume.

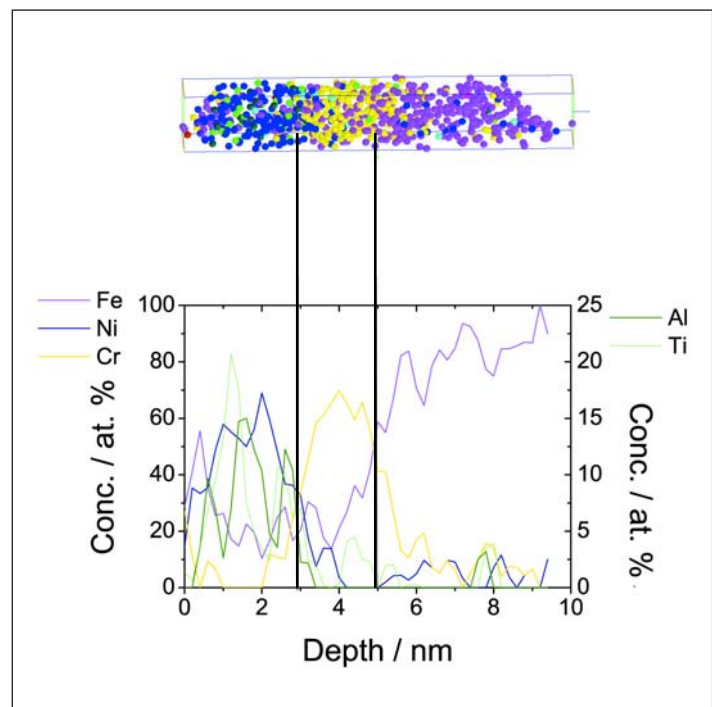


Fig. 3: Concentration depth profiles of Cr, Ni, Al, Ti and Fe through different precipitates and the matrix along the indicated small box shown in Fig. 2 (left end). This box is depicted above the diagram (colours are the same as in Fig. 2, however, Fe atoms (pink) are added).

- [1] A. Gemperle, J. Gemperlova, W. Sha, and G.D.W. Smith, *Mater. Sci. Techn.* **8**, 546–554 (1992).
- [2] W. Sha, A. Cerezo, G.D.W. Smith, *Metall. Trans. A* **24A**, 1241–1249 (1993).
- [3] K. Stiller, M. Hättestrand, F. Danoix, *Acta Mater.* **46**, 6063 (1998).
- [4] K. Stiller, F. Danoix, M. Hättestrand, *Mater. Sci. Eng. A* **250**, 22 (1998).

Pseudo-crystalline ordering of nanoparticles in ferrofluids induced by magnetic fields.

A. Wiedenmann, M. Kammel, A. Hoell

■ HMI, SF3

Ferrofluids are stable magnetic colloids in which nanometre sized magnetic particles are prevented from lumping together either by electrostatic repulsion or by coating with organic chain molecules acting as surfactants. Renewed interest in these materials is motivated by potential biomedical applications such as cancer therapy. Here small amounts of a ferrofluid are injected into the cancerous tissue. A cyclic variation of an external magnetic field then heats the fluid destroying cancer cells usually particularly sensitive to overheating.

Small angle scattering (SAS) is an analytical technique providing statistical information about structures in the nanometre range. It is therefore particularly suited for investigations of such liquids. While X-ray scattering (SAXS) probes mainly the particle core (due to its high electron density), neutron scattering (SANS) gives access to composition and density of the organic shell, the core and the magnetic

particle moments. Spin-polarized neutrons (SANS POL) provide an additional contrast for the magnetic core and allowed mesoscopic constituents of poly-disperse ferrofluids to be identified quantitatively. In very diluted Co-Ferrofluids (The magnetic core consists of cobalt), we were able to evaluate precisely the average radius of the magnetic core of 3.7 nm and the composition of the shell of constant thickness 2.3 nm. Here we focus on the set-up of field induced correlations as a function of the particle concentration, the strength and the orientation of the applied magnetic field and the temperature.

In Fig. 1 the results of SANS-measurements performed on Co-Ferrofluids with non-polarised neutrons in a horizontal magnetic field of 1.1 T perpendicular to the incident beam are shown. The results are presented in the usual form of a SANS-pattern showing the intensity of the scattered beam in dependence of the scatter-

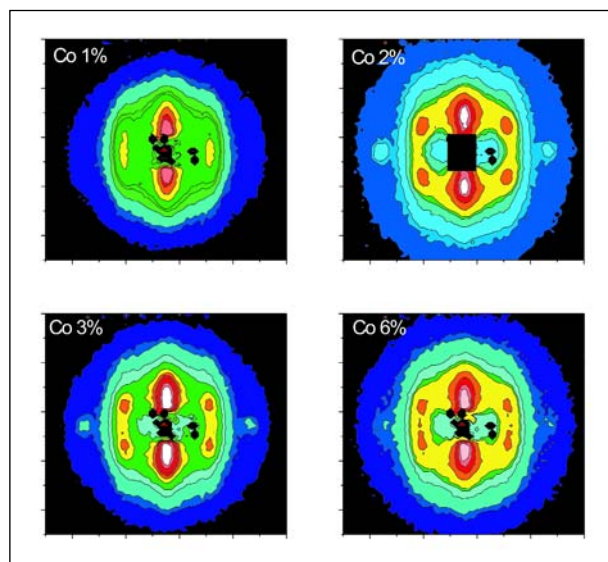


Fig. 1: 2D-SANS pattern of Co-Ferrofluids of different concentrations in a horizontal magnetic field H of 1 T applied perpendicular to incident neutrons: Above 1 vol. % Co well defined peaks (orange spots) represent the pseudo-crystalline hexagonal ordering of particles while below streaks perpendicular to H indicates chain like particle arrangements.

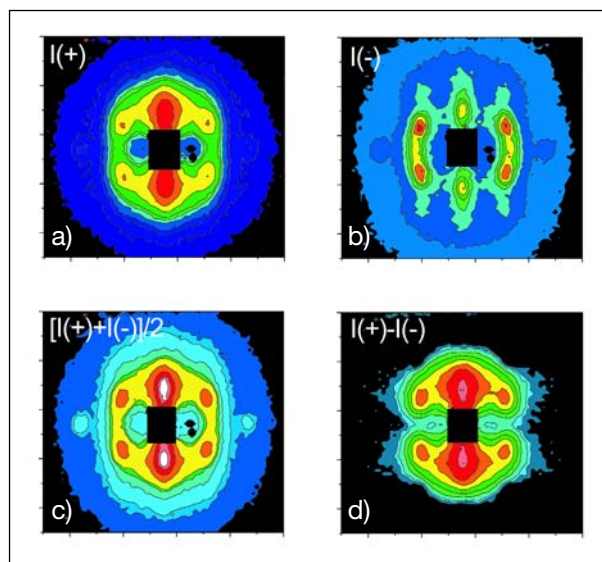


Fig. 2: 2D-SANS POL (SANS with polarized neutrons) intensities for 2 vol % Co-Ferrofluids sample for both neutron polarization directions a), and b) the average corresponds to the pattern of non-polarized neutrons c) and the difference pattern represents the nuclear-magnetic cross-term for one and the same particle (d).

ring vector Q , i.e., essentially in dependence of the direction in which the particles are scattered. In this pattern, different intensities are represented by different colours ranging from blue for low intensities to orange and red for high intensities. In our measurement, we observed pronounced peaks (orange spots) for samples with more than 1 vol. % Co. These peaks – a sign of regular arrangement of the particles – disappeared in zero field.

In Fig. 2, SANS-intensities measured with polarized neutrons are shown. $I(-)$ and $I(+)$ are the results of experiments with the neutron spins parallel and antiparallel to the magnetic field H respectively, are shown in Fig. 2 as a typical example the for 2% Co-Ferrofluids. The average $[I(+)+I(-)]/2$ corresponds to the scattering pattern of non-polarised neutrons while the difference pattern $I(+)-I(-)$ of Fig. 2 reflects the nuclear-magnetic cross term resulting solely from one and the same particle. From Fig. 1 and Fig. 2 four peaks forming angles of $\pm 30^\circ$ with the horizontal direction of the applied magnetic field are clearly distinguished. Two additional peaks in the horizontal direction result solely from nuclear contrast and disappear completely in the cross-term.

A SAXS study performed on the ID01 beamline at ESRF, Grenoble on the same samples in a horizontal magnetic field applied perpendicular to the incident beam fully confirmed the set-up of very narrow peaks with increasing field.

The peaks observed in the small angle scattering experiments correspond to a pseudo-crystalline ordering of the Cobalt particles in an external field. For samples above 1 vol.% Co, inter-particle interactions are induced by an applied magnetic field that gives rise to pseudo-crystalline ordering of Cobalt core-shell particles. The particles are arranged in hexagonal planes, with the magnetic moments parallel to the $[110]$ direction. Two types of equivalent textures were found to be present simultaneously, corresponding to a stacking of the hexagonal planes in vertical (type I) or the horizontal direction (type II). The pseudo-crystalline particle arrangements are schematically shown in Fig. 3.

The in-plane nearest neighbour distance of $a_{hex}=21.9$ nm was found to be almost independent of concentration (and temperature) whereas the distance between neighbour planes strongly varies from sample to sample between $c=70$ nm and 25 nm. The ordering follows the direction of the applied field, i.e. the magnetic moments and the $[110]$ directions are always

aligned along the magnetic field. In addition, the Q^{-1} behaviour of the intensity observed at low scattering vectors in the direction perpendicular to the magnetic field indicates that some particle moments are arranged in the attractive head-to-tail conformation and aligned along the magnetic field presence of segments of uncorrelated chains.

The pseudo-crystalline lamellar hexagonal particle arrangement has never been observed experimentally before in magnetic colloids. This contradicts the theoretical predictions of de Gennes and Pincus that the competition between repulsive (hard-core) and attractive (van-der-Waals) interaction with magnetic dipole-dipole interaction should give rise to a spontaneous arrangement of particles in chains or rings with magnetic moments parallel to each other. In an external magnetic field these chains are expected to be aligned along the field direction.

On the other hand, theoretical studies performed by Hess using molecular dynamics have predicted that above a critical value of the magnetic dipole moment a transition from the uniaxial to a lamellar, symmetry-breaking ordering should occur with almost close-packed in-plane structures. The results presented here confirm for the first time experimentally the transition from field induced chain-like to lamellar ordering.

The work is supported by the German Research Foundation (DFG project No WI-1151).

-
- [1] A. Wiedenmann in Lecture Notes in Physics, ed. S. Odenbach (2002), 33-61.
 [2] A. Wiedenmann, M. Kammel, A. Hoell, P. Boesecke; Phys Rev. E **68** 031203, 1–10 (2003).

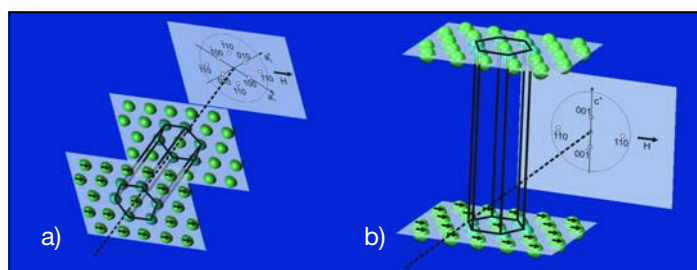


Fig. 3: Schematic representation of particle arrangements in hexagonal symmetry in textures of type I (a) and type II (b) and the corresponding reciprocal lattice points observed in the detector plane. The horizontal magnetic field is perpendicular to the incident beam.

Modification of the Ti Texture using swift heavy ions

I. Zizak¹, N. Darowski¹, G. Schumacher¹, S. Klaumünzer¹; W. Assmann², J. Gerlach³, I. Großhans⁴

■ 1 HMI, SF4 ■ 2 Ludwig-Maximilian-Universität, Munich ■ 3 Leibniz Institute for Surface Modification, Leipzig ■ 4 University of Augsburg

Accelerated ions interact with solids through nuclear and electronic interaction. At very high energies, the nuclear energy loss (S_n) is much smaller than the electronic energy loss (S_e), and the interaction between the ions and the solid leads to excited electrons in the solid. A part of the electronic excitation energy is converted into atomic motion, e.g. via the electron-phonon coupling. This motion can lead to lasting changes in the structure of the irradiated solid.

Recently, a change in crystallite orientation of polycrystalline titanium (Ti) films was detected after the irradiation with 200 MeV gold (Au) ions [1]. In order to study the mechanisms of this texture modification, a new series of experiments was performed at HMI. In the present report, variations of the incoming beam's angle, the irradiation dose, and the grain size of the samples are reported.

The experiment

A bulk Ti sample with an average grain size of approximately 5 μm was compared to fine-grained Ti films deposited on the Si (001) wafer (grain size of the order of magnitude of 100 nm). The thickness of the film was 3 μm . All samples were

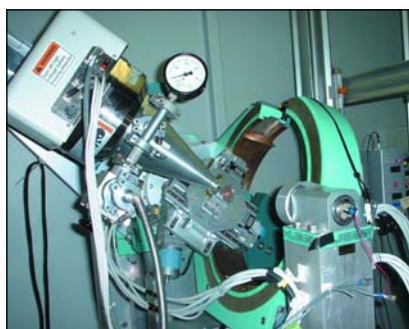


Fig. 1: Improved experimental device used in the investigation of texture changes in thin titanium films with X-rays at BESSY. The figure shows the sample mounted on the goniometer head and the area detector during the measurement. The incoming X-ray beam enters the figure from the right.

cut into 8 × 8 mm² square pieces and uniformly irradiated at room temperature with 350 MeV Au ions up to a fluence of 5 · 10¹⁴ ions/cm². Because the deposited Ti films already possessed a texture, we irradiated the thin samples under two different angles, 20° and 45°, to avoid correlation effects between the ion beam direction and the existing orientation distribution. The textures of irradiated samples were studied using the synchrotron radiation beam at the KMC2 beamline at BESSY [2]. In order to

avoid absorption by the substrate, the diffraction was measured in reflection geometry. The size of the focused beam at the sample position was 200 × 200 μm^2 .

Representation of the results – the pole figure

A pole figure describes the spherical distribution of the crystal lattice planes. In a standard Bragg experiment, the intensity of the diffracted beam is proportional to the volume of the sample irradiated by X-rays, and to the fraction of the planes which are satisfying the Bragg condition, i.e., the plane normal halves the angle between the incoming and diffracted beam. When the sample is rotated in two directions and the measured intensity is mapped versus the sample orientation, the distribution function of the selected planes can be measured.

In the pole figure, the polar angle is projected onto the distance from the center and the azimuthal angle onto the angular distance from the x -axis (pointing from the center to the right). The crystallographic planes which are parallel to the surface give rise to the maximum in the middle of the figure, and the planes whose normal lies in the surface plane will have a maximum on the perimeter of the figure.

Since the unambiguous determination of the crystal orientation in three dimensions requires at least two angles, the orientation distribution function (ODF) requires even in simple cases at least two pole figures of non-parallel plane sets in crystal, so the experiment has to be repeated for another Bragg angle.

Results

In the unirradiated state, the thick sample showed a texture specific for rolled metal sheets. This texture did not change even after irradiation with 5 · 10¹⁴ ions/cm². The grain size seems to have an important influence on introduced grain orientation.

Below $5 \cdot 10^{14}$ ions/cm², the textures of the films showed no changes. First changes became visible above this value and the resulting textures depended on the beam direction. Since already at a dose of about 10^{13} ions/cm² the sample is completely covered with tracks, we conclude that texture modification does not occur in single ion tracks but reorientation of the crystallites requires multiple track overlap.

The rate of texture change was similar for samples irradiated under different incident angles, both textures showed the first changes only above 10^{14} ions/cm². The resulting textures are different, and depend on the ion beam direction.

Fig. 2 shows three sets of pole figures, for an unirradiated thin film, and for thin films irradiated with the maximal dose, $5 \cdot 10^{14}$ ions/cm². There is a maximum in the middle of the (002) and (101) pole figures for all three samples. We already showed in our previous experiment [5] that the Ti layer starts to grow with the (101) plane parallel to the surface, but above a certain thickness it grows with the (002) plane parallel to the surface. We assume that the maximum in the middle (101) pole figure comes from the deeper regions of the film, which are closer to the substrate, and the (002) maximum from the grains nearer to the surface. We also see that the maximum in the middle of the (101) pole figure is not much affected by ions.

The angles 20° and 45° were chosen in such a way that one of them lies below and one above the direction of the (101) plane normal in the unirradiated sample (approximately 27° from surface). If we look at the (002) pole figures of the irradiated sample, we can see that the (002) peak in the 20° sample moves to the left, and in the 45° sample to the right. This behaviour suggests the affinity between the (101) plane normal and the direction of the ion beam. Also, as in the previous experiment [5], a break of the fibre texture into six distinct maxima was observed.

A more quantitative comparison with the previous experiment is difficult due to the different qualities of the Ti layers used in the experiments. Different growing rates and/or tem-

perature resulted in different initial states. Furthermore, a slight difference in the ion energy may cause a variation in the dynamics of the texture alteration.

- [1] H.D. Mieskes, W. Assmann, F. Grüner, H. Kucal, Z.G. Wang, and M. Toulemonde, *Physical Review B* **67**, 155414 (2003).
- [2] A. Erko, I. Packe, C. Hellwig, M. Fieber-Erdmann, O. Pawlitzki, M. Veldkamp, W. Gudat, *AIP Conf. Proc.* **521**, 421 (2000).
- [3] H. Dammak, A. Barbu, A. Dunlop, D. Lesueur, *Phil. Mag. Lett.* **67**, 253 (1993).
- [4] H. Dammak, A. Barbu, A. Dunlop, D. Lesueur, *Phil. Mag. A*, **79**, 147 (1999).
- [5] I. Zizak, N. Darowski, J. Gerlach, A. Wenzel, *ISL Annual Report 2002*, 43.

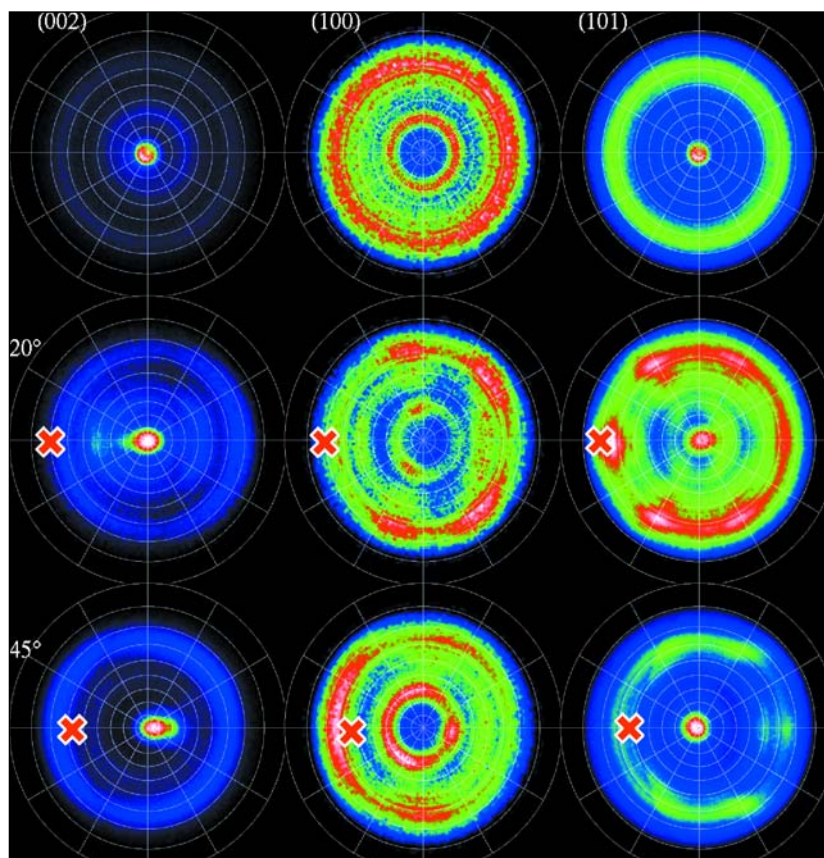


Fig. 2: Pole figures of thin titanium layers: unirradiated sample (top row), irradiated under 20° (middle row) and 45° incident angle. The pole figures show the spherical distribution of the crystal lattice planes with a particular orientation. Here the figures for the crystal planes (002), (100) and (101) are given. The red cross marks the irradiation direction. The comparison of the (101) results for the unirradiated sample and the sample after irradiation under 20° shows that the irradiation led to a recrystallization of the sample with the direction of the ion beam coinciding with the preferred orientation of the crystallites. See text for detailed discussion of the results.

Nonthermal Melting of BeO Films Induced by Swift Heavy Ions

K. Czernski¹, G. Schiwietz¹, M. Roth¹, F. Staufenbiel¹; P.L. Grande²

■ 1 HMI, SF4 ■ 2 Universidade Federal do Rio Grande do Sul, Porto Alegre, Brazil

Introduction

Swift heavy ions passing through a solid lead to a lasting structural change along their paths. The process leading to the creation of these ion-tracks is a central research topic in the field of ion-solid interaction. Spontaneous lattice relaxation was originally proposed by Watson and Tombrello [1] as a possible ion-track formation-mechanism. According to this, a high electronic excitation density induced by swift heavy ions in a solid produces a large internal pressure of the electron gas leading to an expansion and destruction of the crystal lattice. Alternatively, the modification of the electron screening between target ions directly decreases the cohesion of the solid [2] and consequently causes a fast, non-thermal melting within the ion track region. Up to now, this process was observed only for a few semiconductors in pump and probe experiments with femtosecond lasers [3, 4]. The estimated melting time amounted to several hundreds of femtoseconds.

Here we present an evidence of an ultrafast band gap collapse and nonthermal melting of beryllium oxide BeO thin films induced by swift heavy ions and investigated by means of the Auger electron spectroscopy.

The Experiments

The experiments were performed using highly charged argon (Ar), xenon (Xe) and gold (Au) beams from the ISL cyclotron at energies of several MeV per nucleon. We applied a thin carbon foil placed in front of the UHV target chamber to increase the charge states of the projectiles and the energy density deposited in the target. The BeO films of about 10 nm thickness were produced by implanting 500 eV oxygen ions into an atomically clean Be target or alternatively by oxidation of Be under an oxygen atmosphere of about 10^{-7} hPa. To test the targets' quality we measured the KVV (K-valence-valence) Auger electron spectra induced by 2.7 keV electrons from an electron gun mounted at the target chamber. In Fig. 1 a single line with the maximum at 100 eV originating from metallic Be and a multippeak spectrum characteristic for BeO with the main line shifted by about 10 eV towards lower electron energy are presented. The electron beam was focused to a spot size smaller than 1 mm and positioned at the target with a precision of about 0.3 mm. The electron and ion-beam induced Auger-electron spectra were measured by a 45° parallel-plate electrostatic spectrometer located at an angle of 135° with respect to the ion-beam direction.

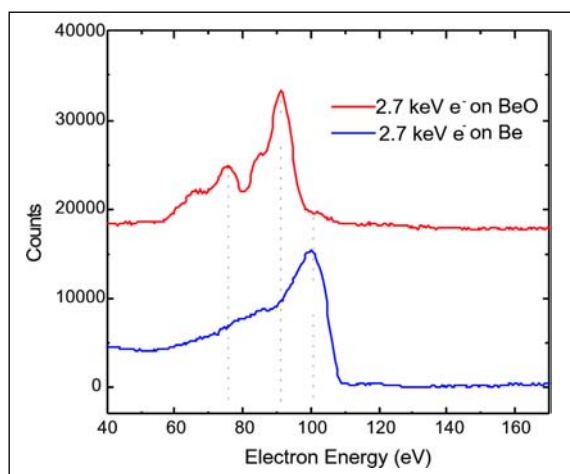


Fig. 1: Electron induced Auger spectra for metallic beryllium (blue) and beryllium oxide (BeO – red)

Auger electron spectra measured during irradiation of BeO thin films by Ar^{7+} , Ar^{15+} and Xe^{31+} ions are depicted in Fig. 2. The lines at energy of about 140 eV correspond to the K^2VV Auger decay arising from double ionization of the K shell. The KVV spectra differ significantly from that obtained repeatedly for the electron incidence (Fig. 1) during the beam time. In addition to the multippeak BeO spectrum, the line characteristic for the metallic Be appears. The strength of the “metallic contribution” increases with increasing stopping power of the projectiles. It is very small for the Ar^{7+} ions whereas it dominates for the Xe^{31+} beam. The spectra obtained for the Au^{41+} incidence [5] show no BeO contribution any more. The broadening of the metallic KVV line compared to the electron induced one results from the increased temperature of the electron gas the time scale of the

Auger decay [6] amounting to about 13 fs. The line broadening coincides with that obtained for irradiation of the metallic Be target [7]. Furthermore, the line positions agree with those observed for the electron incidence. This excludes any ion track potential and thus the Coulomb explosion as the ion-track formation mechanism in BeO.

Discussion

The appearance of the metallic Be Auger line in the spectra of the BeO target is a very remarkable result. It indicates that the electron band-structure of BeO collapses completely already before the Auger decay, i.e. faster than 13 fs. Moreover, the same Auger decay energy of 101 eV for the metallic Be and BeO targets suggests that the cohesion energy and thereby the atomic distances in both cases should be similar. On the other hand, the ionic bonds of BeO are much stronger than those characteristic for the metallic phase. Thus we can conclude that the Auger emission from BeO takes place already after a lattice relaxation to the metallic liquid phase. A simple estimation of the relaxation time based on the known difference in the cohesion energy and bond lengths leads to a value of about 5 fs [5] in agreement with the experimental results. This is about one order of magnitude faster than the similar transition to the metallic phase observed for silicon in the femtosecond-laser irradiation-experiments [4].

Another important experimental result is the observation of the energy-density variation of the insulator-metal phase transition. Similarly to the laser experiments, the phase transition can occur only at a high electronic excitation density that corresponds in ion-beam experiments to a high stopping power value. The onset of the nonthermal melting arises already for the irradiation by Ar^{7+} ions. A saturation of the effect, corresponding to the ultrafast melting the entire region of the ion track, could be reached for Xe^{31+} and Au^{41+} ions.

Outlook

BeO as a wide gap ionic crystal is predestined to study the short time instabilities of the lattice due to dense electronic excitation. However, the relation between the crystal structure and the critical density of electrons in conduction bands within the confined geometry of an ion track should be investigated in more detail. The spontaneous lattice relaxation, because of its short time scale, can be the most effective ion-track formation mechanism for insulators and semiconductors irradiated by swift heavy ions.

- [1] C.C. Watson, T.A. Tombrello, *Rad. Eff.* **89**, 263 (1985).
- [2] P. Stampfli, *Nucl. Instr. Meth. B* **107** (1996) 138; P. Stampfli, K.H. Bennemann, *Phys. Rev B* **46**, 10686 (1992).
- [3] K. Sokolowski-Tinten et al., *Phys. Rev. Lett.* **81**, 3679 (1998); K. Sokolowski-Tinten, D. von der Linde, *Phys. Rev. B* **61**, 2643 (2000).
- [4] S.I. Kudryashov, V.I. Emel'yanov, *JETP Lett.* **73**, 228 (2001).
- [5] K. Czerski et al., *ISL Annual Report 2002*, p. 12.
- [6] G. Schiwietz et al., *Europhys. Lett.* **47**, 384 (1999).
- [7] F. Staufienbiel et al., *ISL Annual Report 2002*, p. 14.

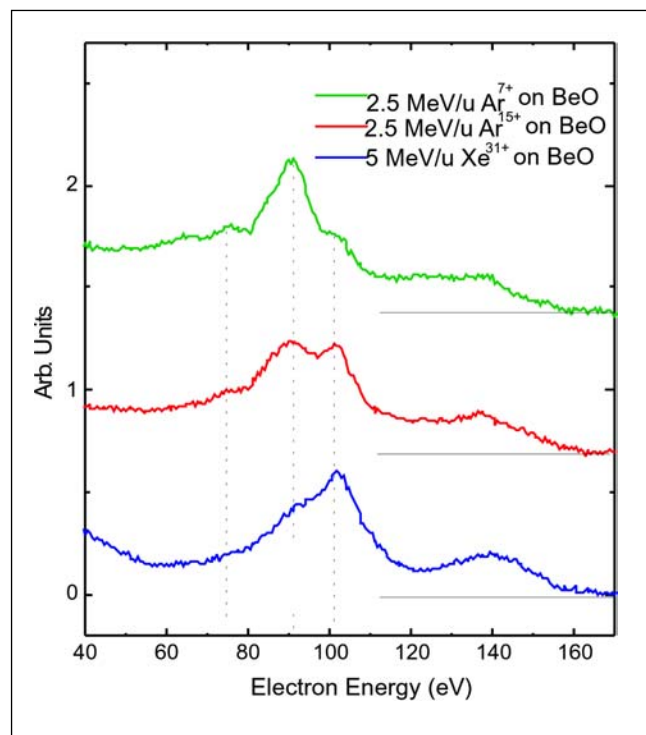


Fig. 2: Ion induced Auger spectra for BeO irradiated with swift heavy ions of different mass and charge state. With increasing mass and charge the peak corresponding to metallic beryllium becomes increasingly prominent, the BeO-peak vanishes (cf. Fig. 1).

TEMPOS – A universal ion track-based electronic building block

D. Fink¹, A. Petrov¹, W. Fahrner², K. Hoppe³

■ 1 HMI, SF4 ■ 2 FernUniversität Hagen, FB Elektrotechnik, Hagen ■ 3 Fachhochschule Südwestfalen, FB Elektrotechnik und Informationstechnik, Hagen

Contemporary electronic structures frequently consist of single crystalline silicon wafers with a dielectric layer (usually silicon oxide or oxy nitride) layer on top. Suppose that these structures are irradiated with swift heavy ions and etched, and the etched tracks there-upon filled with a material of sufficiently high resistivity, then one obtains paths for charge transport between the conducting silicon channel induced below the

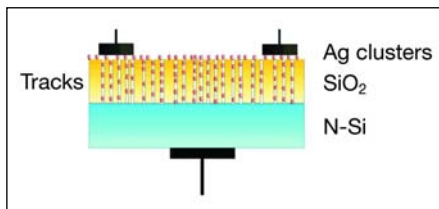


Fig. 1: Principle construction of a TEMPOS structure. In this example a highly resistive layer of dispersed Ag nanoclusters is used as filling material.

oxide, and the surface of that oxide layer. If additionally highly resistive material is deposited onto the oxide surface and connected by two electrodes (denoted in Fig. 2 by “o” and “w”), and simultaneously the silicon wafer backside is contacted by another electrode (“v” in Fig. 2), then one obtains a family of novel electronic elements. Due to their peculiarity to use narrow conducting pores as charge transport paths, these structures have been named TEMPOS which is the abbreviation of *Tunable Electronic Material with Pores in Oxide on Silicon*.

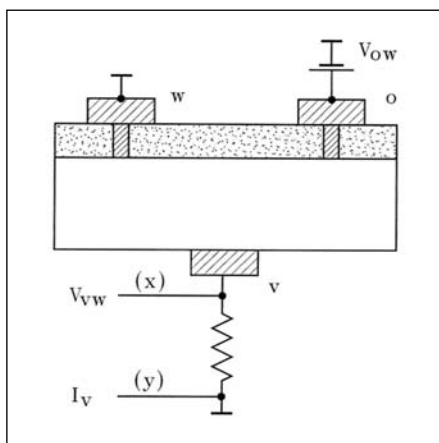


Fig. 2: The TEMPOS symbol adopted by us, and the principle setup of a basic TEMPOS circuit.

oxide, and the surface of that oxide layer. If additionally highly resistive material is deposited onto the oxide surface and connected by two electrodes (denoted in Fig. 2 by “o” and “w”), and simultaneously the silicon wafer backside is contacted by another electrode (“v” in Fig. 2), then

Concerning their electronic behaviour, TEMPOS (patent pending) structures lie in between tunable resistors, capacitors, diodes, transistors, photocells, batteries, and sensors, which explains their universality. Fig. 1 shows the principle construction of these structures, and Fig. 2 shows the corresponding electronic circuit.

The function of these TEMPOS structures is determined by the material and the thickness of the dielectric layer, the diameter, the length, shape and areal distribution of the etched tracks, the type and the distribution of the (semi)conducting matter deposited within these tracks and on the dielectric surface, and of course also by the type of silicon substrate. These many new parameters give rise to unpredicted possibilities. For example, complementary npn and pnp structures can be obtained just by tailoring the track conductivity only (e.g. by different etching times but identical deposition conditions), Fig. 3. In classical silicon electronics, this is possible only by changing the substrate doping.

TEMPOS structures can be easily tailored for special tasks, by adequate choice of the material in the ion tracks and on the sample surface. For example, TEMPOS elements with dispersed silver clusters as highly resistive material can be used as base structures for low frequency noise generators, point-like light emitters, signal frequency amplifiers, low-, high-, and band passes, amplifiers, amplitude modulators, astable multivibrators etc. Further, resistive, conductive and capacitive sensors for temperature and light, photocells, photo-transistors and optocapacitive remote controls of local oscillators have already been realized with this structure.

TEMPOS structures containing fullerite, phthalocyanine, or II/IV semiconductor nano-crystals as highly resistive material show resistive, conductive and capacitive sensoric properties for humidity and gases such as alcohol or acetone.

Circuits have been designed that transform a certain degree of humidity or a certain gas concentration towards frequency, current or voltage, and the corresponding TEMPOS elements can also be used as light, temperature, humidity or alcohol controlled voltage supplies (Fig. 4). At present we test the electronic response of TEMPOS structures upon deposition of new materials in tracks and surfaces, such as of

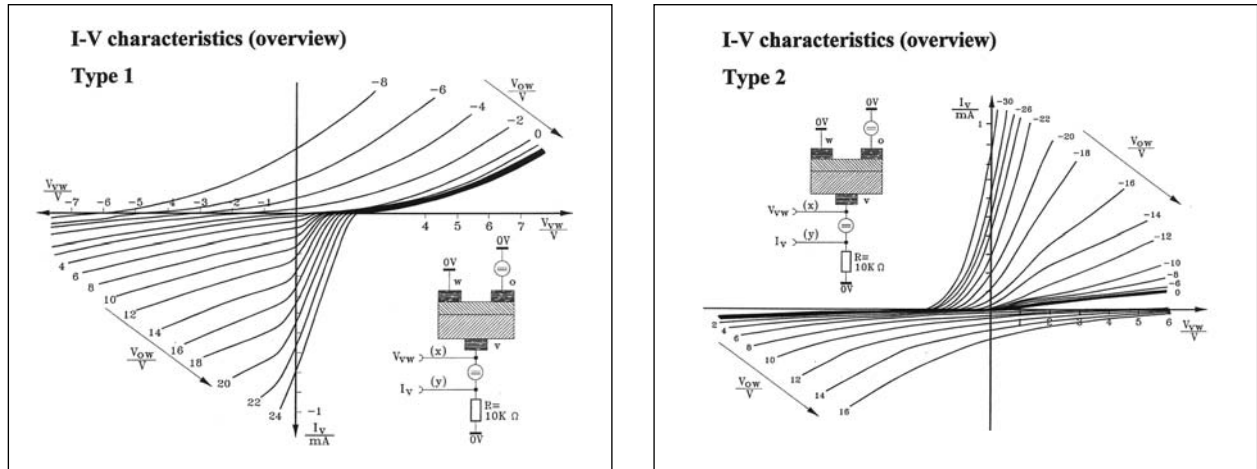


Fig. 3: The two basic types of TEMPOS characteristics, produced by track etching up to different diameters, for the same substrate doping and track filling. **Left:** Type 1 (nnp-Type) after little track etching. **Right:** Type 2 (pnp-Type) after strong track etching. One can also obtain a similar characteristics when keeping the same track diameter but changing the substrate doping.

nanocrystal/polymer composites, with the nanocrystals being as well metals as II/IV compounds. Also the deposition of lithium niobate and of oxides of Zn, Ti and Sn is under examination, and hopefully deposition of buckytubes and ferrofluides in the tracks will follow. When selecting doped polysilane or diamond films as dielectric layers, intrinsically conducting latent tracks with smaller diameters emerge after the ion irradiation, thus enabling higher track densities. It is also intended to fill porous silicon films on TEMPOS structures with adequate matter. The aim of all these works is to develop various types of light emitters and photodetectors and a great variety of sensors with both resistive and capacitive response upon various gases and liquids, upon acoustic and magnetic signals, on upon accelerations and on particle irradiation.

Probably TEMPOS structures are radiation hard as the new additional track of an accidentally impinging highly energetic charged particle will not alter much the behaviour of a structure that already contains some typically 10 millions of conducting tracks/cm².

With ~1000 € being the typical price for one hour beamtime at a heavy ion accelerator with a flux of ~10⁹ ions/s, one can easily estimate that the production of an individual ion track costs around 3 · 10⁻¹⁰ €. This signifies that the cost of irradiation of a silicon wafer of 10 cm diameter – sufficient for producing at least some 1000 TEMPOS structures – will be around ~0.20 €, which is negligible as compared with other production costs. On the other

hand, the cost of production of standard TEMPOS structures will be lowered as, in principle, no doping, no cleanroom, no high vacuum (apart from that in the accelerator), and no lithography is required. For the sake of easy handling in our first experiments, we made our TEMPOS prototypes as large as a few mm in size, but they can, in principle, be diminished considerably. The size of the smallest possible 3-contact-TEMPOS element is given by the distance of two ion tracks, hence is in the order of a few 100 nm to a few μm. Non-gated 2-contact-TEMPOS structures can even restrict to one track only, hence can be reduced down to the 10 nm level.

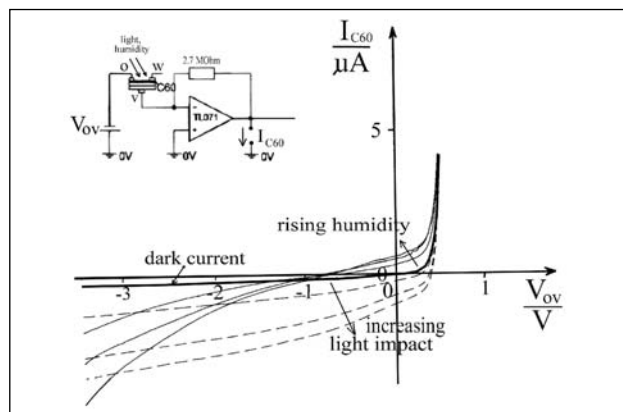


Fig. 4: The change of the DC dark current of a C₆₀-TEMPOS-structure (thick curve) upon visible light impact (day light; dashed curves) or humidity increase (solid thin curves). The presence of alcohol vapor shifts the curve in the same direction as light impact. The measurements shown are performed for zero gating voltage V_{ov}.

Decomposition behaviour of as-received and oxidized TiH₂ powder

B. Matijasevic¹, J. Banhart¹, I. Zizak², N. Darowski², G. Schumacher²

■ 1 Technische Universität Berlin and HMI, SF3 ■ 2 HMI, SF4

Metallic foams are excellent engineering materials offering high energy absorbing capacity, reduced thermal and electrical conductivity, as well as enhanced mechanical and acoustic damping. This material combines properties of cellular materials together with those of metals. The high stiffness-to-mass ratio leads to a variety of applications especially in automotive industry. (See also news report on page 15.)

One very promising and proved way to produce metal foams is the powder metallurgy route [1]. A precursor material tablet is produced by compacting a powder mixture including small amounts of blowing agent powder. Heating of this material causes gas release by decomposition of the embedded blowing agent and thus expansion of the material.

The overall aim is to produce a stabilized blowing agent compatible with the foaming process [2]. The alloy composition and the type of the blowing agent have to be chosen such that the blowing agent gives rise to an ideal foaming behavior with formation of a homogeneous pore size.

Up to now titanium hydride (TiH₂) turned out to be the best foaming agent to reach homogene-

ous pore formation and pore size distribution. As there is a mismatch between the melting point of commercial aluminum alloys and the decomposition temperature of TiH₂ (400°C), the latter should be subjected to thermal and/or oxidizing treatments.

By this an oxide layer is formed on the surface of the titanium hydride powder particles. This layer delays gas release, from the particles, so that during heating up of the powder mixture the blowing first takes place when the melting temperature of the alloy is reached. The thickness and composition of the layer depends of the used temperature and time period of oxidation (Fig. 1).

By the present investigation the influence of various pre-treatments in air on the release of hydrogen from TiH₂ is examined. For this purpose the decomposition of TiH₂ powders is examined by differential scanning calorimetry (DSC) [3], thermogravimetric analysis (TGA) [1,4,5] and mass spectrometry (MS, Fig. 2). The morphology of the powder was obtained by scanning electron microscopy (SEM).

Cold pressed TiH₂ powder pre-heated in air at 520°C for 180 minutes was studied in situ during the heating in air. Synchrotron radiation experiments were performed at the KMC2 beamline at BESSY the synchrotron radiation source in Berlin. Powder diffractometry was performed using an area sensitive detector, which allowed the acquisition of the whole range of the diffraction pattern simultaneously. The sample was mounted on in the focus of a radiation heater (Fig. 3). The temperature of the sample was controlled using two thermocouples mounted on the sample stage. In the preliminary experiment the temperature was changed from room temperature up to 700°C with the constant rate of 5 K per minute.

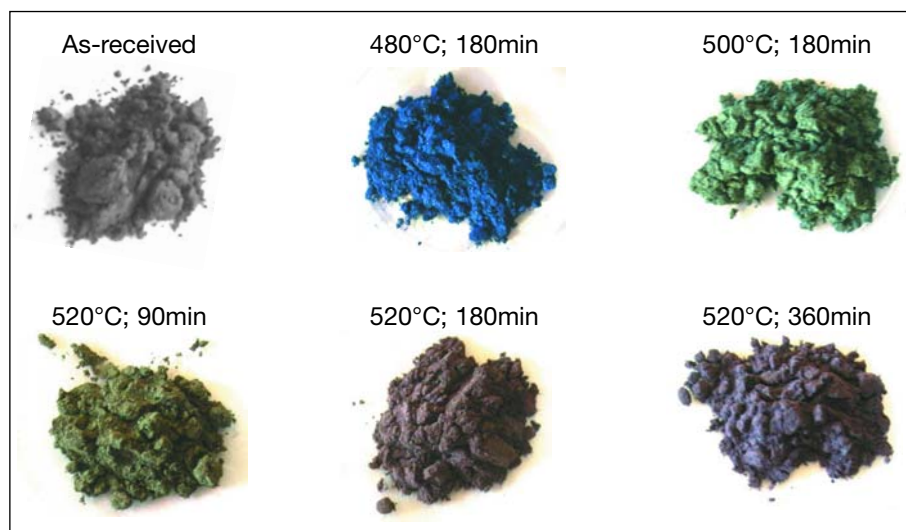


Fig. 1: TiH₂ oxidized at different conditions. The colour of the powder depends on the thickness of the oxygen layer.

The area sensitive detector was covering the angles between 34° and 45° , so it was possible to acquire the most important Bragg reflexes of the different compounds assumed in sample (Fig. 4). Data evaluation showed that we were able to determine the content of hydrogen in the sample and to follow the evolution of the Ti/H ratio using a phase diagram.

We identified the same titanium oxides, which were measured after the pre-treatment on a laboratory X-ray source (see Fig. 4). After the initial change of the TiO_2 intensity, the amount of oxides stayed constant, while the concentration of hydrogen increased considerably. The structure of titanium-hydride changed at higher temperatures to bcc β -phase because of the loss of hydrogen. After the cooling the sample consisted of a mixture of cph α -Ti and fcc δ - $\text{TiH}_{1.5}$. Advantage of the in-situ measurements is the possibility to monitor exactly the phase transition, using only one sample for the whole range of temperatures.

These preliminary in situ X-ray diffraction experiments at BESSY are combined with transmission electron microscopy (TEM) to get some additional information about the structure of the oxide layer covering the hydride particles.

In the future we plan to perform the in-situ diffraction experiment during the pre-treatment of the blowing agent at different temperatures and annealing time, as well as the decomposition of the hydride and in the inert atmosphere.

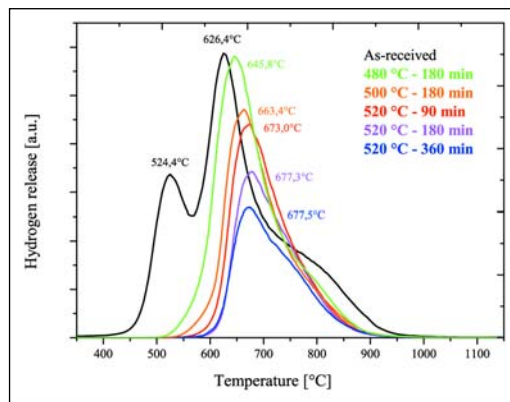


Fig. 2: Release of hydrogen as a function of heat treatment. The decomposition of the TiH_2 is impeded due to the slow diffusion of the hydrogen through the oxide layer.



Fig. 3: The sample was mounted on a ceramic holder and irradiated with a halogen lamp. The incoming X-rays entered the figure from the right-hand side. Scattered photons were reflected through the metal cone on the left side to the detector.

- [1] Baumgärtner F, Duarte I, Banhart J. *Adv Engn Mat* **2**, 168–174 (2000).
- [2] Banhart J. German Patent 100 (15) 2000.
- [3] Centeno-Sanchez RL, Kennedy AR, Wood JV; In: Banhart J, Ashby MF, Fleck NA, editors. *Cellular metals and metal foaming technology*, Bremen: MIT-Verlag (2001) 69–76.
- [4] Gergely V, Clyne TW, In: Banhart J, Ashby MF, Fleck NA, editors. *Metal foams and porous metal structures*, Bremen: MIT-Verlag; (1999) 83–89.
- [5] Kresse R. In: Banhart J, Ashby MF, Fleck NA, editors. *Metal foams and porous metal structures*, Bremen: MIT-Verlag; (1999) 109–112.
- [6] Kennedy AR, Lopez VH, *Mater. Sci. Eng. A* **357**, 258–263 (2003).

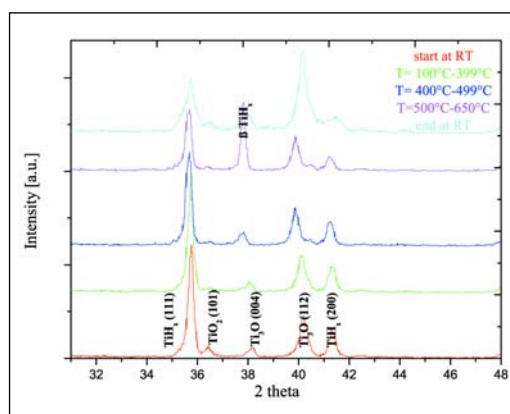


Fig. 4: Alterations of the peak intensities during heating and cooling of a pre-heated powder.

Gelation in suspensions of “sticky” particles

Klaus Kroy
 ■ HMI, SF5

What are gels?

Colloidal gels are (metastable) solids made from small (nm– μm sized) colloidal particles that do not seem to fit very well into the usual classification scheme of the states of matter into (crystalline) solids, liquids, gases, and plasmas. Like for a glass, a snapshot of a gel may resemble a liquid, yet its macroscopic mechanical behaviour is elastic, and therefore it qualifies as a solid. Unlike glasses, gels can moreover exhibit elastic behaviour at extremely low particle densities. These gels then have a ramified (fractal) structure. In a recent collaboration with the Soft Condensed Matter Group of the University of Edinburgh, we argue that the gel state is not so much characterized by its structural properties, but by the fact that it is the result of a kinetic arrest transition [1, 2]. In other words, a gel is not a solid because of certain obvious structural properties – as is usually argued for the common paradigm of a solid, namely a crystal – but simply because upon smoothly varying some (structural) control parameter, its dynamics suddenly became extremely slow. This is in close analogy to the glass transition, and in fact at high densities the critical behaviour at both transitions is theoretically very well described by the same mathematics, known as mode-coupling theory (MCT). For dense fluids giving rise to homogeneous gels (classified as type-I gels in the diagram) this analogy has recently been established by combined theoretical and experimental efforts reviewed in [3].

The classical paradigm revisited

In general, it is not easy to decide whether a system will be in the liquid or in the solid state by simply looking at the system parameters. One might argue that for a solid system an uninterrupted chain of bonded particles needs to percolate throughout the whole sample volume. For (infinitely) strong bonds this is indeed the answer, and the gel transition can be identified with percolation. If the bond energy is not much more than the thermal energy, the answer is less obvious, however. Even if bonds percolate, they are not permanent but only transient. This, on the other hand does not exclude elastic behaviour either. Take a slightly polydisperse glass of hard spheres, for example, without any attraction. At high enough density it undergoes a kinetic glass transition into a “jammed” solid state that obstructs the pathway to optimum packing. Hence, while transient bonds do not guarantee elasticity, elasticity can emerge even without any bonding at all. In the last example polydispersity serves to avoid crystallization, but in other cases gravity or other effects causing extreme slowing-down of crystal nucleation, can effectively lead to the same result.

Figures 1–3: Helen Sedgwick,
 School of Physics, University of Edinburgh

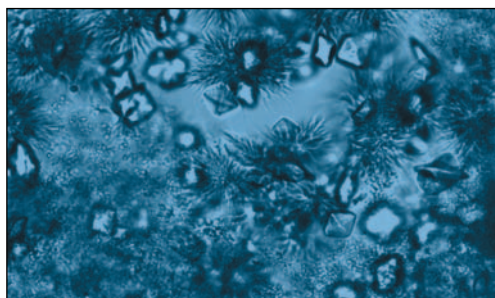


Fig. 1: Optical micrograph showing a transient gel of the globular protein lysozyme formed by the addition of NaCl. Various crystals can be observed to nucleate out of the gel as the gel collapses typically half an hour after formation. (preprint cond-matt/0309616)

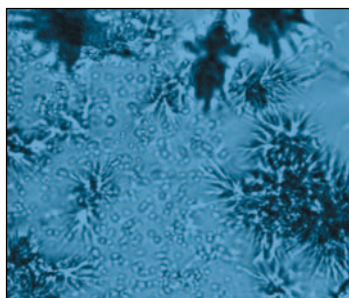


Fig. 2: Optical micrograph showing the non-ergodic homogeneous gel-beads (the small spherical objects) observed in solutions of lysozyme on the addition NaCl, and subsequent crystal nucleation (the larger structures).

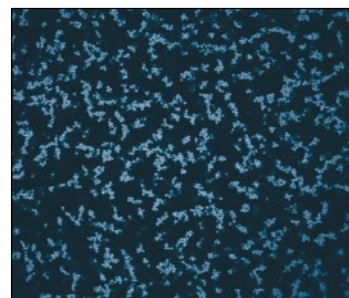


Fig. 3: Confocal micrograph showing the gelation of colloidal particles into ramified aggregates.

Interference of phase separation

Attractive interactions complicate the picture compared to the glass transition of purely hard spheres, because they can induce phase separation into effective liquid and gas phases (the whole colloidal suspension is of course still embedded into a solvent), as familiar from the idealized van-der-Waals fluid. For a range of the attraction less than the particles' hard cores, this gas-liquid phase separation is thermodynamically metastable with respect to crystallization. However, it still dominates the phenomenology since crystal nucleation is comparably slow. It thus becomes important to understand the interaction of liquid-gas phase separation and kinetic arrest. Since both phenomena are kinetic in nature, it is not surprising that this interplay depends on the time scales imposed by external conditions.

Gel classification

Take a dilute solution of nm-sized globular proteins e.g. lysozyme as an example (Figs. 1, 2). To a good approximation the protein interaction can be idealized as that of hard spheres with some short-ranged attraction. The attraction depends on the salt concentration in the solution. When the system is "quenched" into the gas-liquid coexistence region by adding salt to the solution, phase separation into protein-rich drops and an almost pure solvent background occurs. Since the proteins are so small, they diffuse very quickly, so that phase separation proceeds fast relative to the mixing process. Hence gelation in this case can be classified as arising from a "slow quench" leading to gels denoted as type II gels and to gel beads (see diagram and Fig. 2) at low protein volume fractions. Such are the gels that typically plague protein crystallographers, and a better understanding of their physical origin may hopefully guide them in devising more rational protocols. Although they may later crystallize, the crystals formed are not necessarily suitable for x-ray analysis (Fig. 2). For the comparably "large", micron sized colloids, on the other hand, phase separation kinetics may well be slow compared to the time scale for switching on the attractions. In contrast to the situation for the small proteins, in this case gelation is due to a "rapid quench" and produces type III gels and at low volume fractions (and in presence of spurious long range repulsions) fractal clusters (see diagram and Fig. 3).

Type-II gels are homogeneous on short scales but strongly heterogeneous at the mesoscale: they result when the characteristic coarsening textures produced by phase separation get "frozen in" during the coarsening process, as a result of an MCT-like arrest of the denser phase [2]. In contrast type-III gels are assemblies of long-lived

nonequilibrium structures locally resembling those obtained from irreversible cluster aggregation (cf. Fig. 3) and thus heterogeneous also on short scales. To distinguish from fully irreversible aggregates, in which the bonds formed are permanent, the type III process is sometimes called "weak gelation". The underlying speculative view of gelation as a double ergodicity breaking (on the monomer scale and on the cluster scale) [1] seems indeed to be supported by recent numerical simulations [4].

- [1] K. Kroy et al. *A cluster mode-coupling approach to weak gelation in attractive colloids*. Phys. Rev. Lett. (2004) (in the press).
- [2] H. Sedgwick et al. *Non-equilibrium behavior of lysozyme solutions: beads, clusters and gels*. cond-mat/0309616.
- [3] K. N. Pham et al. *Multiple glassy states in a simple model system*. Science **296** (2002) 104.
- [4] E. Del Gado et al. *A unifying model for chemical and colloidal gels*. Europhys. Lett. **63** (2003) 1.

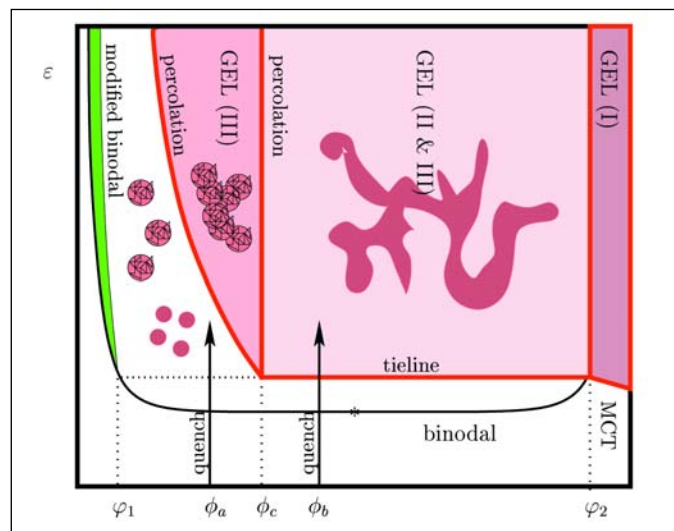


Diagram: Schematic cut through the phase diagram of adhesive hard spheres along a plane spanned by volume fraction ϕ and attractive strength ϵ . The interaction of gas-liquid phase separation with MCT-kinetic arrest leads to a variety of metastable gel phases. At high colloid volume fractions ϕ , where MCT can be applied directly, homogeneous gels form (region I). At lower ϕ phase separation may create macroscopically heterogeneous gels (region II) and homogeneous gel beads if the quench is slow (cf. Figs. 1, 2), while more tenuous gels (regions II & III) and ramified clusters consisting of non-equilibrium particle aggregates result from rapid quenches (cf. Fig. 3). The predicted critical behaviour at the transition is that of percolation along the vertical gel boundaries, while mode-coupling critical behaviour is expected across the tie-line or MCT-line. (cond-mat/0403684)

“VV dip” in light-scattering of supercooled liquids experimentally confirmed

Thomas Franosch
 ■ HMI, SF5

Glass-forming liquids exhibit the striking property of a strong temperature dependence of transport coefficients such as viscosity. A small decrease of temperature by, say, 10 K can induce a factor of 10 in viscosity. The underlying dynamical process that deals with the strong steric hindrance in the molecular motion of the dense liquid is referred to as structural relaxation.

Light scattering has been the ideal tool to investigate these processes, since the dynamical window of these experiments allows one to monitor the evolution of structural relaxation in the temperature range where the liquid changes its behaviour from a viscous liquid to an elastic solid. The theory of light scattering in supercooled liquids was well worked out for liquids at high temperatures but failed to describe the transition to low-temperature amorphous solid.

Recently a collaboration of the Theoretical Physics group of the Hahn-Meitner Institute extended the description of long-wavelength dynamical processes in moderately supercooled liquids, see Ref. [1, 2]. The extension includes a generalization of the elasto-optical Pockel's coupling used in the theory of elasto-dynamics to highly viscous fluids exhibiting a slow structural relaxation in the frequency window of light-scattering. Elasto-optical coupling implies that a molecular liquid is found to respond to shear flow by partial alignment of the molecular axis giving rise to the phenomenon of flow birefringence. A theoretical consideration based on Onsager's reciprocity theorem reveals that this effect has an inverse effect, viz. a steady change of the molecular orientation causes a mechanical shear stress in the liquid. Both effects are consistently described by the same mechanism via the translation-rotation coupling.

For light-scattering experiments the time-dependent thermal fluctuations of the dielectric tensor are the cause of the frequency shift of the scattered beam with respect to the incident one. Since the dielectric properties change upon a local expansion or compression of the liquid as well as upon aligning the axis of a fraction of the molecules, a strong coupling to the hydrodynamic modes is expected. The new aspect of our recent work has been to include the translation-rotation coupling in the description of the light-scattering spectra. The expected spectrum within this approach differs in important respects from the commonly used model. The new feature is an effective frequency-dependent optical coupling mediated by the appearance of the translation-rotation coupling that connects density fluctuations, i.e. phonons propagating through the liquid, to dielectric fluctuations.

As a result of the extension of the theory by translation-rotation coupling, the Brillouin resonance corresponding to the acoustic-like excitation is decorated with an effective frequency-dependent light-matter coupling, thereby slightly modifying the spectral shape of the resonance seen by polarized light scattering with respect to methods sensitive to density fluctuations only.

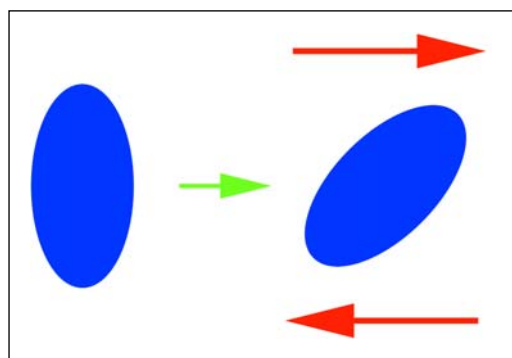


Fig. 1: Molecular alignment by shear flow

The prediction we have made for a weighted difference spectrum of polarized and backscattering depolarized spectra was a small but measurable negative contribution for a certain range of temperatures.

This feature cannot be explained within the conventional approach since it entirely relies on the translation-rotation mechanism. We have therefore proposed to use a simple test to quantify the importance of translation-rotation coupling by searching for the possibility of a negative region of the mentioned difference spectrum.

Recently the experimental group H.Z. Cummins in New York started to remeasure light-scattering of Salol [3, 4], one of the most prominent glass-forming liquids used in the field. The new experiment was necessary to achieve high-precision data in order to perform the difference spectra proposed above. The data for 90 degrees polarized scattering are shown in Fig. 1 and exhibit the thermal evolution of the Brillouin resonance upon incremental supercooling. The difference with respect to the reference depolarized backscattering data is plotted in Fig. 2. The negative contribution (called VV dip by the authors) for a range of temperatures at the low-frequency tail of the resonance is clearly observable and nicely demonstrates the implications of translation-rotation coupling at least for this particular liquid. The experiment constitutes a milestone since it gives evidence that the approaches commonly used have to be reconsidered.

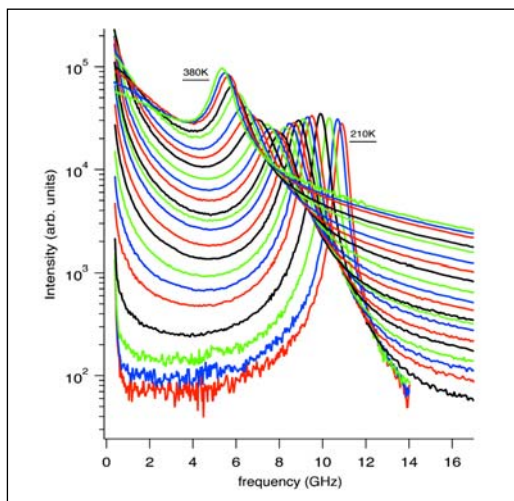


Fig. 2: Polarized Brillouin scattering data at 90 degrees scattering angle of Salol for different temperatures.

The authors of Ref. [3, 4] also carefully analyzed their data within our recently developed theory and found full compatibility with our results. The theoretical considerations thus provided a qualitative and quantitative description of Salol where earlier approaches fail in both respects.

- [1] *Light scattering by longitudinal acoustic modes in molecular supercooled liquids I: phenomenological approach*, R.M. Pick, T. Franosch, A. Latz, and C. Dreyfus, Eur. Phys. J. B **31**, 217 (2003).
- [2] *Light scattering by longitudinal acoustic modes in molecular supercooled liquids II: Microscopic Derivation of the Phenomenological Equations*, T. Franosch, A. Latz, and R.M. Pick, Eur. Phys. J. B **31**, 229 (2003).
- [3] *Brillouin Scattering Study of Salol: Exploring the Effects of Rotation-Translation Coupling*, H. Zhang, A. Brodin, H.C. Barshilia, G.Q. Shen, H.Z. Cummins, R.M. Pick, submitted to Phys. Rev. Lett. (2004).
- [4] *Brillouin Scattering Study of Salol: Exploring the Effects of Rotation-Translation Coupling*, H. Zhang, A. Brodin, H.C. Barshilia, G.Q. Shen, H.Z. Cummins, R.M. Pick, Phys. Rev. E (2004) in press.

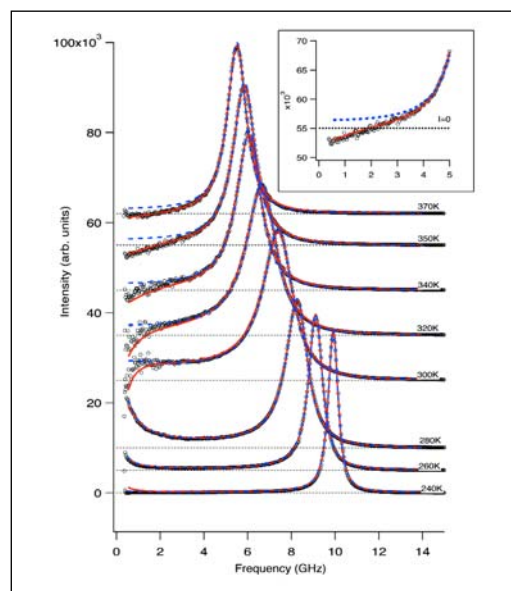


Fig. 3: Difference spectra of Salol for different temperatures. Solid lines are fits to the theory of [1, 2]. Broken lines are fits to a density-fluctuation only model.

Trace elements in the protection of the respiratory tract

K. Bukalis, A. Kyriakopoulos, D. Behne

■ HMI, SF6

The surface of the organs of the respiratory tract, trachea and lungs, is continuously exposed to gases and particulate matter present in the atmosphere. As many of these pollutants are powerful oxidants, these tissues need specific protection against oxidative processes. Several enzymes with key roles in the antioxidative defense system are known to contain metals and metalloids such as copper, iron, manganese, selenium and zinc as essential constituents of their active centers. In addition,

there may be further protective trace-element containing proteins not yet known. It is therefore of great interest to identify these compounds and to find out about their biological functions.

A first series of experiments has been carried out on the lung of the rat to analyze the trace elements present and to obtain information on their chemical forms and on their possible sites of action within the different cell compartments.

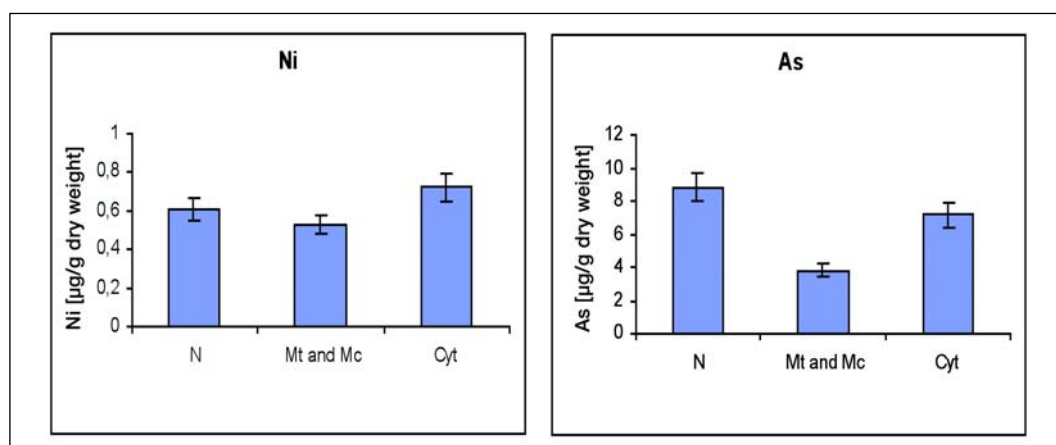


Fig. 1: Concentration of nickel and arsenic in the cytosolic (Cyt), mitochondrial and microsomal (Mt and Mc) and nuclear (N) fractions in the lung of rats.

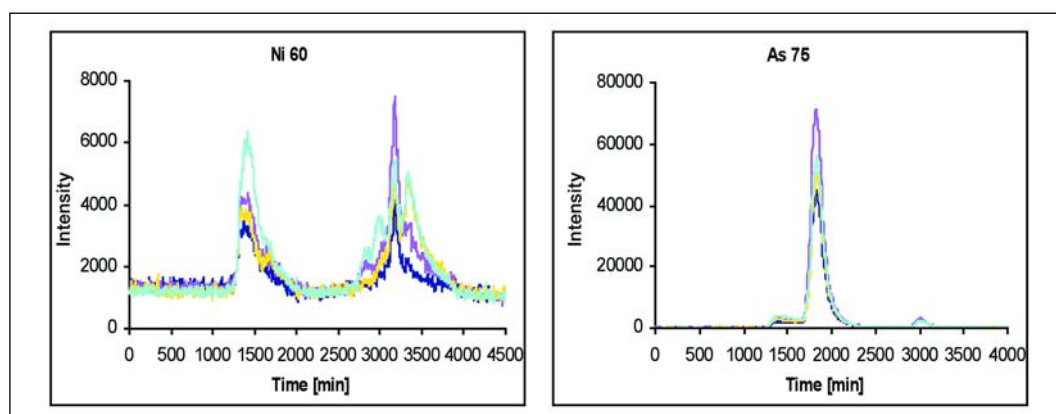


Fig. 2: Distribution profiles of nickel and arsenic after chromatographic separation of lung cytosol.

In these studies element analytical methods and radiotracer techniques have been combined with biochemical separation procedures. Subcellular separation of the tissues into the nuclear, cytosolic, mitochondrial and microsomal fractions has been achieved by differential ultracentrifugation. Instrumental neutron activation analysis (INAA) and graphite furnace atomic absorption spectrometry (GFAAS) have been used to determine the concentrations of several trace elements in the lung and in the subcellular fractions. After separation of the cytosolic proteins by size exclusion chromatography (SEC), mass spectrometry using an inductively coupled plasma (ICP-MS) has been employed to obtain first information on the trace element-containing proteins present in this compartment. The selenium-containing proteins in the whole organ and in the subcellular fractions have been investigated by labeling of rats *in vivo* with ^{75}Se , gel electrophoretic separation of the proteins and autoradiographic detection of the tracer.

The use of the different microtechniques of element analysis allowed the quantitative determination of several trace elements such as arsenic, cobalt, copper, iron, manganese, nickel, selenium and zinc. Of special interest was the high concentration of arsenic which in the lung exceeded those in the liver by a factor of 4 and the fact detected here for the first time that both arsenic and nickel were present in relatively high amounts in the lung cell nuclei (Fig. 1).

The chromatographic fractionation of the proteins present in the liquid cytosolic phase of the lung cells and determination of the element distribution in the separated protein fractions by means of ICP-MS indicated that all the elements investigated were bound to proteins. Copper, iron, manganese, selenium and zinc are known to be essential constituents of redox-active enzymes, but there is the possibility that in the lung these elements may also be contained in further proteins not yet identified. As shown in Fig. 2, arsenic and nickel were likewise found to be protein-bound. So far nothing is known about interactions between these elements and lung proteins. However, the fact that both elements are enriched in this organ and are found in distinct proteins fractions suggests the existence of specific arsenic- and nickel-containing proteins rather than an accidental non-specific uptake. Further studies are therefore needed to investigate more closely the biological functions of these elements and especially the role of arsenic and nickel in this organ.

The most detailed information has been obtained on the selenium-containing proteins after labeling of rats *in vivo* with ^{75}Se , as here, by means of gel electrophoresis in conjunction with the autoradiographic measurement of the ^{75}Se -labeled proteins, high resolution protein separation could be combined with the very low detection limits of the radiotracer technique (Fig. 3). About 24 selenium-containing proteins with molecular masses in the range between 10 and 80 kDa (1 kDa = 1000 amu) could be distinguished in this way in the subcellular fractions. Several selenoenzymes with redox-functions have so far been identified and it is most likely that the selenoproteins play an important specific role in the antioxidative protection of the respiratory system.

The investigations carried out so far have indicated that numerous metal- and metalloid-containing proteins are present in the lung and may be involved in the protection against oxidative stress. More information will be obtained in studies on animal and human tissues and cell cultures which are at present in progress.

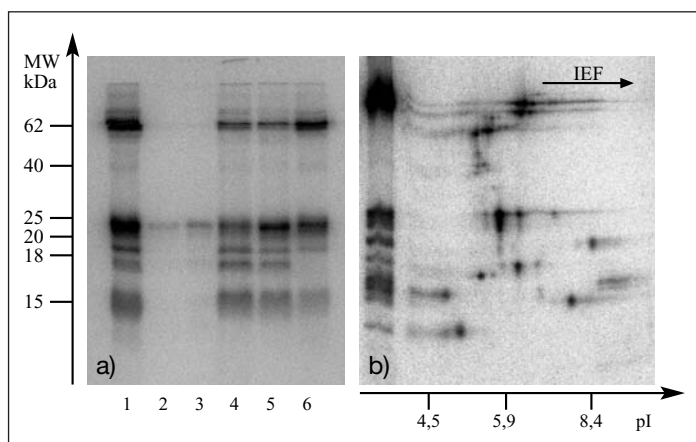


Fig. 3: Autoradiogram of the ^{75}Se -labeled proteins in the homogenate (1) and nuclear (2, 3), mitochondrial (4), microsomal (5) and cytosolic (6) fractions of the rat lung after Laemmli-SDS-PAGE (a) and in the homogenate of the rat lung after IEF/SDS-PAGE (b)